The Astrophysical Journal, 766:21 (17pp), 2013 March 20 doi:10.1088/0004-637X/766/1/21

MULTI-WAVELENGTH STUDY OF A COMPLETE IRAC 3.6 μm SELECTED GALAXY SAMPLE: A FAIR CENSUS OF RED AND BLUE POPULATIONS AT REDSHIFTS 0.4–1.2

J.-S. Huang[1,2], S. M. Faber[3], C. N. A. Willmer[4], D. Rigopoulou[5], D. Koo[3], J. Newman[6], C. Shu[7], M. L. N. Ashby[2], P. Barmby[8], A. Coil[9], Z. Luo[7], G. Magdis[5], T. Wang[2,10], B. Weiner[4], S. P. Willner[2], X. Z. Zheng[11], and G. G. Fazio[2]

[1] National Astronomical Observatories, Chinese Academy of Sciences, Beijing 100012, China
[2] Harvard-Smithsonian Center for Astrophysics, 60 Garden Street, MS65, Cambridge, MA 02138, USA
[3] University of California Observatories/Lick Observatory, University of California, Santa Cruz, CA 95064, USA
[4] Steward Observatory, University of Arizona, 933 North Cherry Avenue, Tucson, AZ 85721, USA
[5] Department of Astrophysics, Oxford University, Keble Road, Oxford OX1 3RH, UK
[6] Department of Physics and Astronomy, University of Pittsburgh, 3941 O'Hara Street, Pittsburgh, PA 15260, USA
[7] Shanghai Key Lab for Astrophysics, Shanghai Normal University, 100 Guilin Road, Shanghai 200234, China
[8] Department of Physics and Astronomy, University of Western Ontario, 1151 Richmond Street, London, ON N6A 3K7, Canada
[9] Department of Physics and Center for Astrophysics and Space Sciences, University of California, San Diego, 9500 Gilman Drive, La Jolla, CA 92093, USA
[10] School of Astronomy and Space Science, Nanjing University, Nanjing, China
[11] Purple Mountain Observatory, Nanjing, China
Received 2012 July 18; accepted 2012 December 4; published 2013 March 4

ABSTRACT

We present a multi-wavelength study of a 3.6 μm selected galaxy sample in the Extended Groth Strip (EGS). The sample is complete for galaxies with stellar mass $>10^{9.5}$ $M_{\odot}$ and redshift $0.4 < z < 1.2$. In this redshift range, the Infrared Array Camera 3.6 μm band measures the rest-frame near-infrared band, permitting nearly unbiased selection with respect to both quiescent and star-forming galaxies. The numerous spectroscopic redshifts available in the EGS are used to train an artificial neural network to estimate photometric redshifts. The distribution of photometric redshift errors is Gaussian with standard deviation $\sim 0.025(1+z)$, and the fraction of redshift failures ($>3\sigma$ errors) is about 3.5%. A new method of validation based on pair statistics confirms the estimate of standard deviation even for galaxies lacking spectroscopic redshifts. Basic galaxy properties measured include rest-frame $U-B$ colors, B- and K-band absolute magnitudes, and stellar masses. We divide the sample into quiescent and star-forming galaxies according to their rest-frame $U-B$ colors and 24–3.6 μm flux density ratios and derive rest K-band luminosity functions and stellar mass functions for quiescent, star-forming, and all galaxies. The results show that massive, quiescent galaxies were in place by $z \approx 1$, but lower mass galaxies generally ceased their star formation at later epochs.

Key words: cosmology: observations – galaxies: distances and redshifts – galaxies: evolution – galaxies: luminosity function, mass function

Online-only material: color figures

1. INTRODUCTION

The central puzzle of galaxy evolution is how baryons fall into galaxies and turn into stars. Understanding the mass assembly history of galaxies is a critical element for solving this puzzle. Galaxies can be generally divided into two populations: those actively forming stars and those that are quiescent with relatively little star formation. Observationally, these two types of galaxies have differing colors corresponding to different regions in color–magnitude (CM) diagrams (Strateva et al. 2001; Hogg et al. 2003). The star-forming galaxies are said to occupy the "blue cloud" (BC), while the passive galaxies occupy the "red sequence" (RS). Similar bimodal distributions are also seen in their morphologies, spectral types, metallicities, and star formation rates (SFRs; Madgwick et al. 2003; Kauffmann et al. 2003a, 2003b). Morphologically most galaxies in the RS are elliptical/S0 galaxies, and galaxies in the BC are disk or irregular/peculiar galaxies. This bimodality is observed over a very wide redshift range up to $z \lesssim 2.5$ (Bell et al. 2004; Willmer et al. 2006; Faber et al. 2007; Brammer et al. 2009). In a color–stellar-mass diagram, red galaxies appear to be much more massive than blue ones.

Formation of massive red galaxies cannot be accounted for by any simple blue-to-red galaxy evolution path. Many authors (Toomre & Toomre 1972; Toth & Ostriker 1992; Kauffmann et al. 1993; Cole et al. 1996; Hopkins et al. 2006) suggest that galaxy merging is the only way to form massive red galaxies. There are probably more than two merging scenarios: two blue galaxies can merge to trigger a burst to star formation and eventually form a massive red galaxy, or two blue galaxies can evolve to red galaxies, then undergo a dry merging to form a massive galaxy. A census of red and blue galaxies at different redshifts is needed to constrain how galaxies migrate from the BC to the RS.

Redshifts are essential for studying galaxy populations. Early spectroscopic galaxy surveys (Lilly et al. 1995; Cowie et al. 1996; Lin et al. 1999; Cohen et al. 2002) usually obtained several hundreds of redshifts. These surveys concluded that strong galaxy evolution seen in faint B-band galaxy counts was mainly due to blue galaxy evolution since $z = 1$ with red galaxies showing little or no evolution. Im et al. (2002) constructed luminosity functions (LFs) for elliptical galaxies in $0.5 < z < 1$ with the DEEP1 redshift sample and argued that they saw only passive luminosity evolution but no change in number density for elliptical galaxies since $z = 1$. These early redshift surveys are too small to have significant statistics for massive red galaxies, which can also suffer a large cosmic variance (Somerville 2005). Recently several large optical redshift surveys have been carried out on 8 m class telescopes including VIMOS VLT Deep Survey (VVDS; Le Fèvre et al. 2005), zCOSMOS (Lilly et al. 2007), and DEEP2 (Faber et al. 2007; Davis et al. 2007), each with more than 10,000 redshifts

available for galaxies at $0 < z < 1.5$. These redshift surveys are highly complete for blue galaxies up to $z = 1.4$ because the [O II] λ3727 line can be observed. Measuring redshifts for red galaxies is more difficult because there are only absorption lines available in most of their spectra, and at high redshifts, only luminous red galaxies can have redshifts measured in these existing redshift surveys. Therefore, optical redshift samples suffer severe bias against red galaxies at high redshifts.

Most studies of evolution of galaxy populations have used optically selected samples. Several groups (Bell et al. 2006; Faber et al. 2007) used photometric or photometric/spectroscopic combined redshift samples to study the evolution of red galaxies and found that the number density of red galaxies increases from $z = 1$ to $z = 0$. This is consistent with a migration of galaxy population from BC to RS. However, as mentioned above, optically selected samples are biased against red galaxies at $z \sim 1$, where even the *I* band probes the rest-frame UV.

Near-IR-selected galaxy samples permit detection of red galaxies with lower luminosities or at higher redshifts (Brammer et al. 2009; van Dokkum et al. 2009) than optically selected samples. The rest-frame *K*-band light of a galaxy comes mainly from M and K stars and traces underlying stellar mass (Cowie et al. 1996; Huang et al. 1997; Bell & de Jong 2001). Therefore, a rest-frame *K*-band-selected galaxy sample is equivalent to a mass-selected sample unbiased against either red or blue galaxies, permitting fair statistics for both galaxy populations. However, early ground-based near-infrared (NIR) surveys have been ineffective because of small format IR array camera and high NIR sky background. Large-format NIR array cameras on 4–8 m class telescopes now allow deep NIR surveys with both wide coverage and faint limiting magnitude $K_{\rm AB} \approx 23$–25 mag (Cimatti et al. 2002; Franx et al. 2003; Bundy et al. 2006; Taylor et al. 2009; van Dokkum et al. 2009; McCracken et al. 2010). Most deep *K*-band surveys focus on formation and evolution of passive red galaxies with $M_* > 10^{11}\ M_\odot$ at $z \sim 2$ (Franx et al. 2003; Taylor et al. 2009; Brammer et al. 2009; van Dokkum et al. 2009; McCracken et al. 2010). On the other hand, local *K*-band galaxy surveys detect early-type galaxies with stellar masses as low as $10^{9.5}\ M_\odot$ (Cole et al. 2001; Bell et al. 2003). More recently, Baldry et al. (2012) estimated the local stellar mass function down to $M_* = 10^7\ M_\odot$ and found that the local stellar mass function has a very steep slope at the lower mass end. Most relevant to the present study, Bundy et al. (2006) carried out *K*-band imaging in the Extended Groth Strip (EGS) region with $K_{\rm AB} < 23$. The limiting stellar mass for their *K*-selected sample is $\sim 10^{10.5}\ M_\odot$ at $z \sim 1$. Formation and evolution of lower mass red galaxies since $z = 1$ have not yet been well studied.

The Infrared Array Camera (IRAC) on board the *Spitzer Space Telescope* can perform very fast scanning of the IR sky with great depth. The IRAC 3.6 and 4.5 μm bands probe the rest NIR for galaxies at $z \sim 1$. There are several large, deep IRAC surveys. Samples obtained in these surveys are usually confusion limited at $f_\nu \approx 1\,\mu$Jy. The limiting flux of $1\,\mu$Jy ($[3.6] = 23.9$[12]) corresponds to an absolute *K*-band magnitude of $M_K = -19$ for a galaxy at $z = 1$. A galaxy with $[3.6] = 23.9$ mag has a typical *R*-band magnitude of 26 (Barro et al. 2011), too faint for spectroscopy even with 8 m class telescopes. Photometric redshifts are essential in studying faint mid-infrared (MIR) selected galaxies.

[12] In this paper, the notation $[w]$ means the AB magnitude at wavelength w in μm. Some other papers have used this notation to mean Vega magnitudes.

Using photometric redshifts is inevitable in studying red galaxy evolution. With large-format CCD cameras available on 6–8 m class telescopes, deep multi-wavelength photometric data became available. These data permit measurement of accurate photometric redshifts for much larger samples of faint galaxies than can be obtained spectroscopically. A difficulty is that for galaxies at higher redshifts, the dominant features in galaxy spectral energy distributions (SEDs), for example, the Balmer/4000 Å break, shift out of the visible band. Including intermediate-band photometry can improve the photometric redshifts (Wolf et al. 2003; Ilbert et al. 2009), and accuracy can be further improved by extending the wavelength coverage to the NIR. Recently the NEWFIRM intermediate-band survey, including three bands in the 1.2 μm window and two bands in the 1.6 μm window, was completed with the NOAO 4 m telescope in search of passive galaxies at $z > 1.5$ (Whitaker et al. 2011). The relative redshift uncertainty $\sigma_z/(1+z)$ for their photometric redshifts is 1%–2% for the *K*-selected galaxies.

To extend SED fitting to the *Spitzer* IRAC bands, photometric redshift estimation must overcome a new challenge: variation of point-spread function (PSF) from ultraviolet to mid-infrared. Traditionally, photometric redshift estimation (Rudnick et al. 2001; Brodwin et al. 2006; Ilbert et al. 2006, 2009) is performed by fitting a set of templates to an observed galaxy SED obtained in a multi-wavelength photometric survey. PSF variation in different bands may distort the observed SEDs (Labbe et al. 2005), and anyway we have poor knowledge of galaxy SED templates in the MIR (Lu et al. 2003; Brodwin et al. 2006). Artificial neural networks (ANNz; Collister & Lahav 2004) is an alternative redshift estimation method. ANNz has several advantages for MIR-selected galaxy samples: it does not require any knowledge of galaxy SED templates, and the resulting photometric redshifts are not affected by photometry offsets caused by PSF variation or any other systematic offset in different bands. ANNz uses a calibration sample to set up an empirical relation between spectroscopic redshifts and observed galaxy properties. Input parameters can be anything including color, flux, size, and even digital morphological parameters. All this method requires is that input and calibration samples have the same filter set for photometry and cover the same input parameters and redshift ranges. Though ANNz cannot measure any redshift beyond the range of the calibration sample, Brodwin et al. (2006) showed that ANNz photometric redshifts for an MIR-selected sample have much smaller scatter than those derived with the SED template methods.

This paper presents a multi-wavelength study of a complete 3.6 μm selected galaxy sample at $z < 1.2$ in the EGS region. Photometric redshifts for this sample are derived using ANNz. Section 2 describes the sample selection, and Section 3 explains the photometric redshift derivation with ANNz including the uncertainties. Section 4 gives results for the blue and red galaxy populations at $0.4 < z < 1.2$ and their properties including the rest *K*-band LF and CM relation. Section 5 summarizes results. Source distances are based on standard flat Λ cold dark matter cosmology with $H_0 = 70$ km s^{-1} Mpc and $\Omega_{\rm M} = 0.30$.

2. THE 3.6 μm SELECTED SAMPLE IN EGS

The All-wavelength Extended Groth Strip International Survey (AEGIS; Davis et al. 2007) is a large multi-wavelength survey in bands from the X-ray (Laird et al. 2009) to 20 cm (Ivison et al. 2007). The original *Chandra* survey covers the whole strip ($2^\circ \times 15'$) with 200 ks per pointing, and later the central $45' \times 15'$ strip with a deeper exposure of 800 ks per

Table 1
Summary of EGS Optical and Infrared Photometry Used for Photo-z Estimation[a]

Band	Telescope	Depth	Survey
u	MMT	26.1	MMT/Megacam EGS Area Survey (Zhao et al. 2009)
u'	CFHT	25.7	Canada–France–Hawaii Telescope Legacy Survey (CFHTLS)
g	MMT	26.7	MMT/Megacam EGS Area Survey Zhao et al. (2009)
g'	CFHT	26.5	Canada–France–Hawaii Telescope Legacy Survey (CFHTLS)
B	CFHT	25.7	DEEP2 CFHT Imaging
$F606W$	*HST*	26.9	*HST* Imaging
r'	CFHT	26.3	Canada–France–Hawaii Telescope Legacy Survey (CFHTLS)
R	Subaru	26.1	Subaru Imaging (Zhao et al. 2009)
R	CFHT	25.3	DEEP2 CFHT Imaging
i'	CFHT	25.9	Canada–France–Hawaii Telescope Legacy Survey (CFHTLS)
i	MMT	25.3	MMT/Megacam EGS Area Survey (Zhao et al. 2009)
I	CFHT	24.9	DEEP2 CFHT Imaging
$F814W$	*HST*	26.1	*HST* Imaging
z'	CFHT	24.7	Canada–France–Hawaii Telescope Legacy Survey (CFHTLS)
z	MMT	25.3	MMT/Megacam EGS Area Survey (Zhao et al. 2009)
J	Palomar	22.9	Bundy et al. (2006)
K_s	Palomar	22.9	Bundy et al. (2006)
K_s	Subaru	23.7	T. Yamada (2010, private communication)
IRAC 3.6 μm	*Spitzer*	23.9	*Spitzer* GTO+GO (X. Z. Zheng et al., in preparation)
IRAC 4.5 μm	*Spitzer*	23.9	*Spitzer* GTO+GO (X. Z. Zheng et al., in preparation)
IRAC 5.8 μm	*Spitzer*	22.3	*Spitzer* GTO+GO (X. Z. Zheng et al., in preparation)
IRAC 8.0 μm	*Spitzer*	22.3	*Spitzer* GTO+GO (X. Z. Zheng et al., in preparation)

Note. [a] For the complete photometry data available in EGS, see Barro et al. (2011).

pointing. The X-ray limiting flux densities[13] for the 200 ks imaging in the whole strip are 5.3×10^{-17} erg cm^{-1} s^{-1} in the soft (0.5–2 keV) band and 3.8×10^{-16} erg cm^{-1} s^{-1} in the hard (2–10 keV) band (Laird et al. 2009). Ivison et al. (2007) performed a deep radio imaging at 1.4 GHz in the EGS region with the 5σ limiting flux density of 50 μJy. Both X-ray and radio can help identify active galactic nuclei (AGNs). More recent data include *Herschel Space Telescope* FIR/submillimeter imaging in the EGS as part of the HerMES survey (Oliver et al. 2010; Roseboom et al. 2012; Smith et al. 2012). The SPIRE 5σ limiting flux densities are 13.8, 11.3, and 16.4 mJy (Oliver et al. 2012). The angular resolution for the SPIRE images are 18″, 25″, and 36″ at 250, 350, and 500 μm; sources are blended in the EGS SPIRE images. Deep 24 μm imaging is available in the EGS region (Dickinson et al. 2007) with the 5σ limiting flux density of $f_{24} = 20\,\mu$Jy, providing a good prior to identify the blended *Herschel* SPIRE sources. The actual FIR photometry catalog in the Advanced Camera for Surveys (ACS) covered area was extracted using the MIPS 24 μm catalog as the prior with the method described in Roseboom et al. (2012). D. Rigopoulou et al. (in preparation) derived FIR luminosities for *Herschel* sources in the region by fitting templates to their IR SEDs.

The EGS also has a large number of spectroscopic redshifts available (Davis et al. 2003; Faber et al. 2007; Cooper et al. 2011, 2012).[14] The AEGIS data sets include one of the deepest IRAC surveys, covering $10'\times2^\circ$ with $\gtrsim$9 ks exposure time. The IRAC observations, data reduction, and photometry were presented by Barmby et al. (2008) and later with more aggressive source extraction by X. Z. Zheng et al. (in preparation). The latter authors found 80% completeness at limiting flux densities of 1.8 and 2.0 μJy, respectively, at 3.6 μm and 4.5 μm compared to ~60% completeness at these flux densities found by Barmby et al. For the current paper, we have restricted our sample to the *Hubble Space Telescope* (*HST*) ACS imaging region ($10'\times1^\circ$; Lotz et al. 2008), where there are generally deeper visible and NIR photometric data available. Our preliminary sample includes all objects in this region with flux density $f_{3.6} > 2\,\mu$Jy in the Zheng et al. catalog. This limit selects galaxies over a wide redshift range and also a few stars. There are 23,327 objects in the preliminary sample.

The visible and NIR photometric data for the sample are summarized in Table 1. There are 18 bands from u to 8 μm that are useful for photometric redshifts. Figure 1 shows a histogram of the number of photometric points available per object. About 96% of the objects have photometry in at least five bands, and 62% of the objects have data in at least 15 bands. As Table 1 shows, however, some of the visible and NIR bands are redundant. For example, there are four versions of R-band imaging with various depths. In redundant bands, we used a σ-weighted mean to combine photometry to give a single photometric value with maximum signal-to-noise ratio in each band. After combining redundant bands, there are 12 wavelengths available in the u–8 μm range. In the visible range *ugriz*, the Canada–France–Hawaii Telescope Legacy Survey (CFHTLS; Ilbert et al. 2006) provides a well-calibrated photometry system, and we transformed all photometry in this wavelength range into the CFHTLS system.

This study focuses on galaxy population at $0.4 < z < 1.2$ to take advantage of the large number of spectroscopic redshifts available. Therefore, the preliminary all-z sample needs to be refined by rejecting foreground stars and background galaxies at $z > 1.2$. A set of simple color criteria can separate the background galaxies. Huang et al. (2004) and Sorba & Sawicki (2010) show that the IRAC [3.6]–[4.5] color is a function of redshift (Figure 2): galaxies with [3.6]–[4.5] < 0 are at

[13] The limiting flux density is defined as the flux to which at least 1% of the survey area is sensitive (Laird et al. 2009).
[14] http://deep.berkeley.edu/DR3/

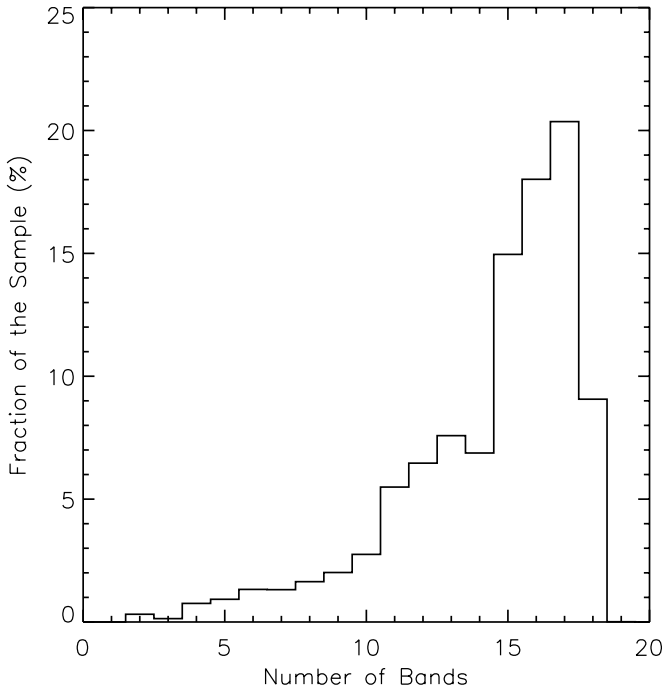

Figure 1. Histogram of number of detections in the multi-wavelength data set. There are a total of 18 photometric bands available for the sample.

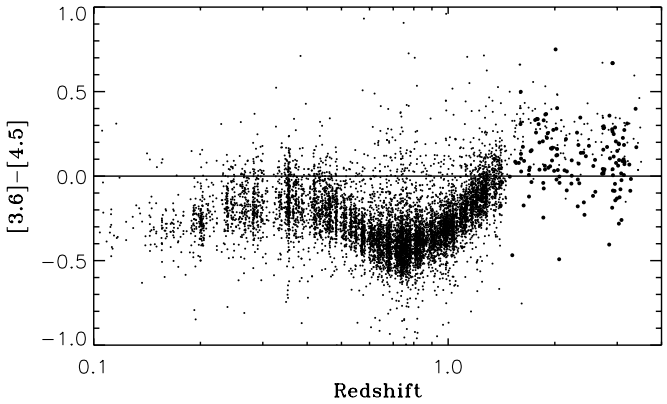

Figure 2. IRAC [3.6]–[4.5] colors as a function of redshift. All galaxies in the preliminary sample, i.e., before the color cuts of relations 1–3, are shown. The fine dots denote the DEEP2 galaxies, and bigger dots denote BM/BX galaxies and LBGs detected by IRAC (Steidel et al. 2003, 2004; Shapley et al. 2005; Huang et al. 2005; Rigopoulou et al. 2006) and MIPS 24 μm selected ULIRGs at $z \sim 2$ (Huang et al. 2009). The line at [3.6]–[4.5] = 0 separates galaxies at $z \approx 1.5$: galaxies with smaller redshift have bluer [3.6]–[4.5] color.

$z < 1.25$, and galaxies with [3.6]–[4.5] > 0 are at $z > 1.25$.[15] This is because 1.6 μm bump in galaxy SEDs shifts through the IRAC bands at $z > 1$. Several groups have used this SED feature to select galaxies at $z \approx 2$ for *Spitzer* Infrared Spectrograph spectroscopy with a nearly 100% successful identification rate (Weedman et al. 2006; Faber et al. 2007; Huang et al. 2009; Desai et al. 2009; Fadda et al. 2010). Some rest-frame UV-selected galaxies at $2 \lesssim z \lesssim 3$ such as BM/BX galaxies and Lyman break galaxies (LBGs), however, are too young to have developed the 1.6 μm bump (Huang et al. 2005; Rigopoulou et al. 2006), and these galaxies may have [3.6]–[4.5] < 0 even with $z > 1.2$. We therefore need an additional criterion to reject these young blue galaxies. We used an optical–MIR color–color diagram ($R - I$ versus $R - [3.6]$, Figure 3) for classification. Figure 3 shows that stars, galaxies at $z < 1.25$, and galaxies at $z > 1.25$ occupy different regions. Thus the three criteria for selection of the 3.6 μm galaxy sample are as follows:

$$[3.6] - [4.6] < 0, \quad (1)$$

$$R - I > 0.2(R - [3.6]) + 0.015, \quad (2)$$

$$R - I < 0.4(R - [3.6]) + 0.5. \quad (3)$$

Criterion 1 removes background galaxies with a normal 1.6 μm bump, criterion 2 rejects young, blue galaxies at $z > 1.25$, and criterion 3 rejects stars. Criterion 1 is not as stringent as that proposed by Sorba & Sawicki (2010) for the same purpose, and thus may reduce the bias by the color cut, but will include galaxies at $z \geqslant 1.3$ in the preliminary sample. These galaxies will be rejected from the sample after we apply criterion 2. Criterion 2 is very similar to the *BzK* selection for galaxies at $z \sim 2$, but used here to reject these galaxies. Ilbert et al. (2009) used their SED-fitting photometric redshift sample to demonstrate that galaxies can be well separated at $z = 1.3$ in the same $R - I$ versus $R - [3.6]$ diagram.

By combining both criteria 1 and 2, we can effectively reject galaxies at $z > 1.25$ while reducing the bias caused by applying only one color criterion. The final sample for photometric redshift estimation includes objects in the *HST*/ACS area of the EGS meeting the above three criteria and with [3.6] < 23.15. Figure 4 confirms that our sample selection does not have any strong bias against either quiescent or star-forming galaxies. There are 12,890 galaxies in the final sample.

Figure 5 illustrates successive application of the color criteria. In our preliminary sample, 95% of the objects have both *R*- and *I*-band detections and can be selected by all three criteria.

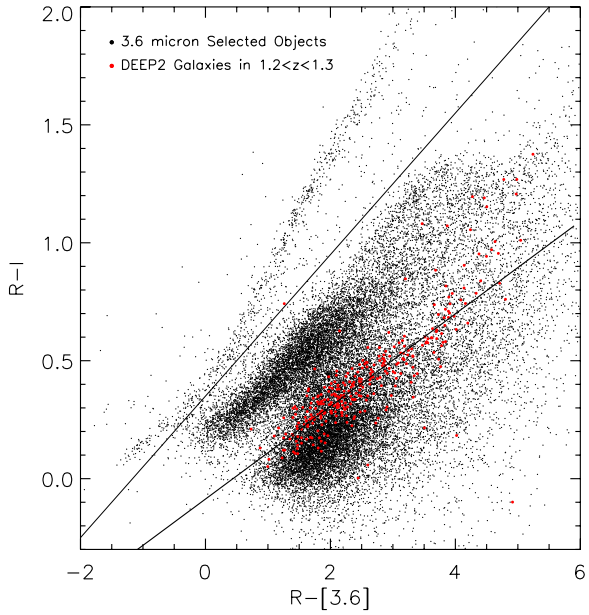

Figure 3. Visible-IR color–color diagram. Points denote all objects selected in the 3.6 μm preliminary sample; red points denote galaxies with spectroscopic redshifts between 1.20 and 1.30. Lines show the color cuts of relations 2 (lower line) and 3 (upper line). The final sample contains only objects in the middle zone of this diagram.

(A color version of this figure is available in the online journal.)

[15] The exact redshift for galaxies with [3.6]–[4.5] = 0 is weakly dependent on galaxy spectral types with red galaxies having $z = 1.25$ and blue galaxies having $z = 1.50$. Sorba & Sawicki (2010) proposed a more stringent color-dependent criterion to separate galaxies at $z = 1.3$: [3.6]–[4.5]=0.12([3.6]−[8.0])−0.07.

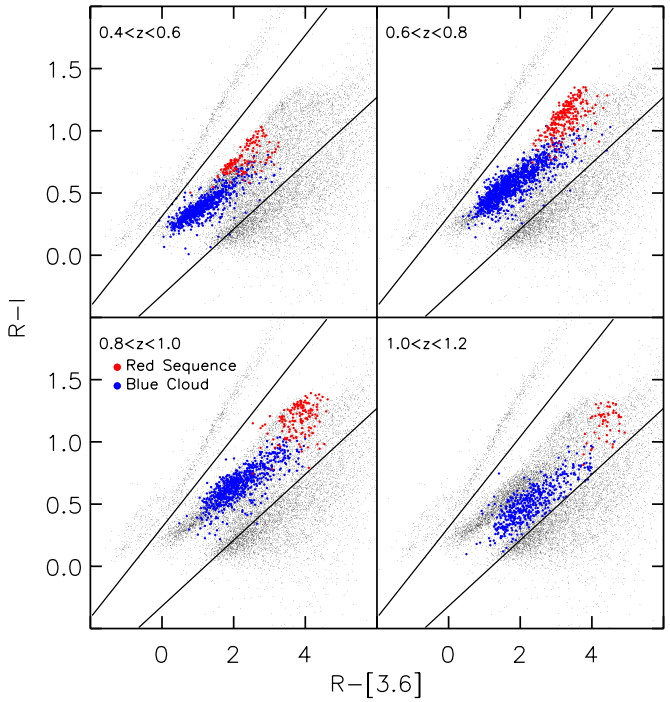

Figure 4. Visible-IR color–color diagram for objects with redshifts and spectral classifications. The locus of the preliminary sample is indicated in gray. Red and blue points indicate galaxies in, respectively, the red sequence and blue cloud in the redshift bins indicated in each panel.

(A color version of this figure is available in the online journal.)

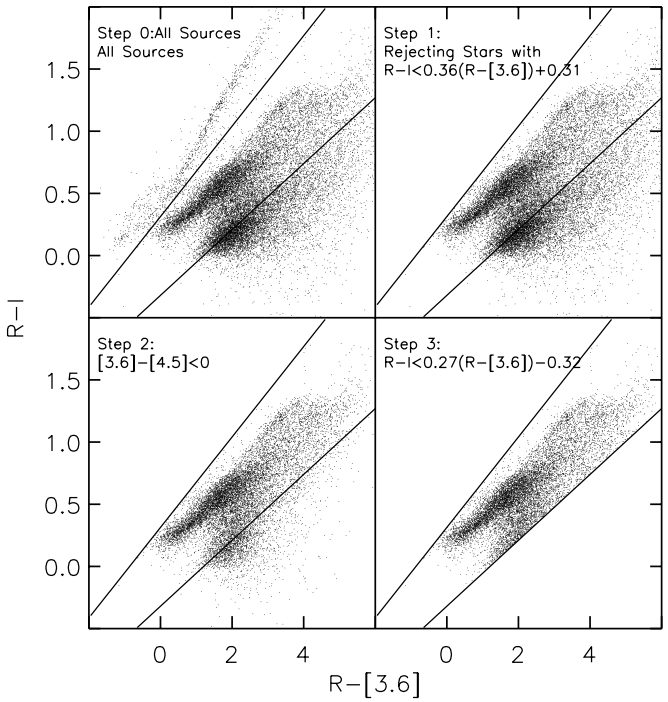

Figure 5. Montage of visible-IR color–color diagrams as sample selection criteria are successively applied. The upper left panel shows all sources in the preliminary sample. The panel to its right shows removal of stars via relation 3. The lower left panel shows removal of most $z > 1.25$ galaxies via relation 1, and the final panel shows removal of the rest via relation 2.

Of the 1297 sources missing either R or I, 1185 have 4.5 μm counterparts which we will be able to classify with relation 1: 387 with [3.6]−[4.5] < 0 are included in the sample and 798 with [3.6]−[4.5] > 0 are rejected. The remaining 112 sources cannot be definitively excluded and are kept in the sample, but their photometric redshifts will be more uncertain than sources having better wavelength coverage.

Our selection does not particularly discriminate against AGNs, but AGNs with power-law SEDs in the mid-infrared band. Objects with strong hot dust emission are called "power-law" objects with a very much red color of [3.6]−[4.5] > 0 even at $z < 1$ (Stern et al. 2005). Thus, their 3.6 μm flux densities for these power-law objects are mainly from hot dust emission, but no longer trace their stellar mass. Huang et al. (2007) found that the number of power-law objects is less than 1% of $>L_*$ galaxies in an 8 μm selected sample. The 3.6 μm band is less sensitive to power-law objects than the 8 μm band; thus, their fraction is even lower in the 3.6 μm selected sample. These objects will be rejected from the sample by criterion 1.

3. PHOTOMETRIC REDSHIFT ESTIMATION

The ANNz method uses a subsample with known redshifts as a training set to build up an empirical relation between measurable parameters and redshifts and then applies this relation to the rest of the sample to derive their photometric redshifts (Firth et al. 2003; Brodwin et al. 2006). Almost any measurable parameter of galaxies including magnitude, surface brightness, color, size, and morphology can be used as an input node for ANNz, but magnitudes at a range of wavelengths are the most common. ANNz requires that the training set should cover the same ranges as the photometric sample in all input parameters. In other words, ANNz cannot derive photometric redshift for a galaxy with input parameter values beyond the range of its training set. The spectroscopic redshift sample has a limiting magnitude of $R < 24.1$, but a significant number of objects in our sample are fainter than this limit. Using magnitudes as input parameters to train the ANNz will allow it to derive photometric redshifts only for galaxies with $R < 24.1$. We therefore used colors with 3.6 μm photometry as the color base as the input nodes in the ANNz estimation. There are 11 non-redundant colors for each galaxy as shown in Table 1. Faint galaxies ($R > 24.1$) at $z < 1.25$ exhibit the same color range as the galaxies with spectroscopic redshifts shown in Figure 6, and therefore the program will be able to derive photometric redshifts for the whole sample.

ANNz network architecture can be described as $N_{\rm input} : N_1 : N_2 : \ldots : N_m : N_{\rm output}$, where $N_{\rm input}$ is the number of input colors for each object. For the present data, $N_{\rm input} = 11$, the number of non-redundant colors. N_1, N_2,..., and N_m are the number of nodes in each ANNz hidden layer for a total of m layers, and $N_{\rm output}$ is the number of sets for output photometric redshift, usually set to be 1. Firth et al. (2003) did extensive experimenting with ANNz to determine the optimal number of hidden layers for the best photometric redshifts and found that a multi hidden layer architecture yields photometric redshifts with a lower $\sigma(z_p - z_s)$ than a single hidden layer architecture. A large number of layers, however, do not significantly improve photometric redshifts. Firth et al. (2003) adopted 6:6:6:6:1 as their fiducial architecture. We ran ANNz with various architectures for our sample and arrived at the same conclusion. The final redshifts use 11:8:8:8:1 architecture, meaning eleven input colors, three hidden layers with eight nodes in each layer, and one output.

The accuracy of the ANNz photometric redshifts is partly determined by the number of objects in the training set. Firth et al. (2003) used a sample of 20,000 objects to show that a larger training set can yield more accurate photometric

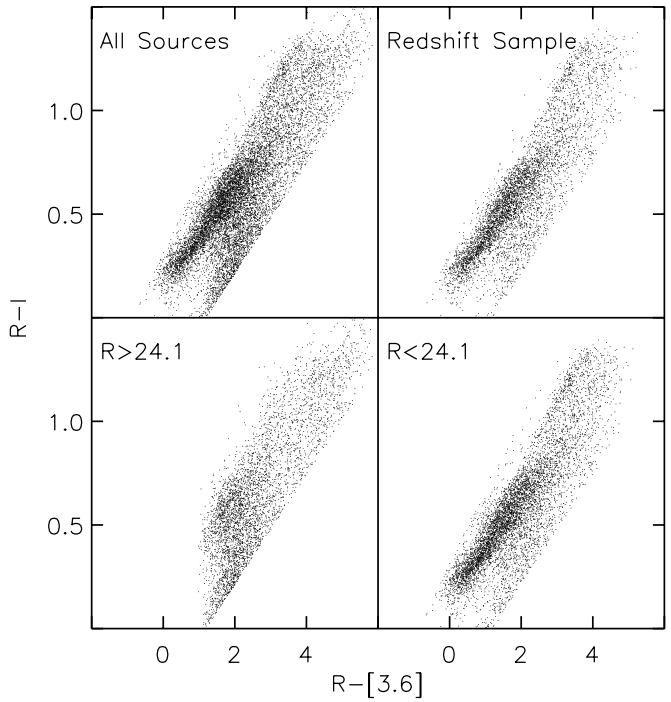

Figure 6. The color–color diagrams for the whole 3.6 μm selected sample, the spectroscopic, faint ($R > 24.1$), and bright ($R < 24.1$) subsamples. The limiting magnitude for the DEEP2+3 spectroscopic survey is $R = 24.1$. This diagram shows that faint objects with $R > 24.1$ in the sample cover the same color range as the objects with spectroscopic redshifts, and we are able to estimate photometric redshifts for these optically faint objects with the spectroscopic subsample as the training set in ANNz.

redshifts, but increasing training set size beyond $n_{\rm train} = 1000$ did not improve the accuracy significantly. There are ~5400 spectroscopic redshifts available in the sample. We divided the spectroscopic redshift subsample into three data sets: a training set, a validation set, and an independent validation set. The first two sets are required by ANNz, and the last one is used to give an independent photometric redshift validation.

Any bad entries, either bad photometry or bad spectroscopic redshifts, should not be included in the training set. Including these outliers will yield large scatters for the resulting photometric redshifts. We ran the ANNz estimation twice. After the first run, we compared photometric redshifts with spectroscopic redshifts in the sample and flagged those with $|z_p - z_s|/(1 + z_s) > 3\sigma_p$.[16] For a second training run, we updated the training and validation sets omitting flagged objects, about 3.5% of the initial sample. This iteration improved the accuracy of the photometric redshifts significantly as shown in Figures 7 and 8.

It is critical to assess the accuracy of photometric redshifts before using them. Traditionally, objects with spectroscopic redshifts are used to evaluate photometric redshift errors. ANNz requires one validation set of objects, and we created an independent subsample with spectroscopic redshifts, none of which is used for ANNz training, for an additional validation. The comparison between photometric and spectroscopic redshifts in Figure 7 permits a direct estimation of photometric redshifts errors. The photometric redshifts derived in the first run show much more systematic deviations caused by the bad redshifts in the training set. Figure 8 shows a Gaussian distribution of

[16] We define σ_p, the calculated uncertainty of the photometric redshifts, as the dispersion of $\delta z_p \equiv (z_p - z_s)/(1 + z_s)$.

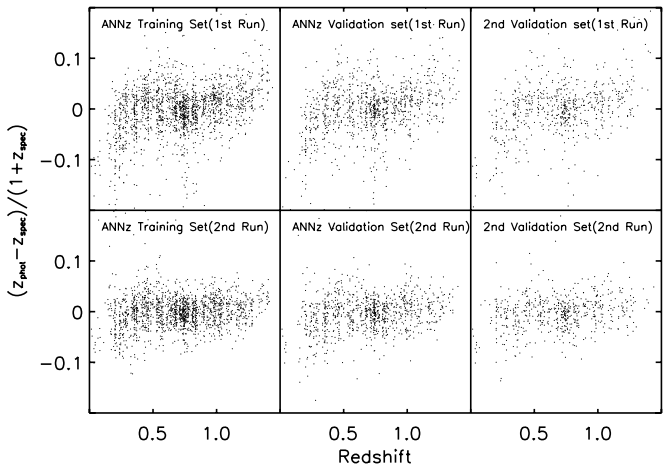

Figure 7. Direction comparison between photometric and spectroscopic redshifts. Panels left to right show the $(z_{\rm phot} - z_{\rm spec})/(1 + z_{\rm spec})$ distributions as a function of redshift for the training, validation, and independent validation samples, respectively. Upper row shows the first ANNz estimation run, and the lower row shows the second run with flagged galaxies removed, which shows much less systematic deviations.

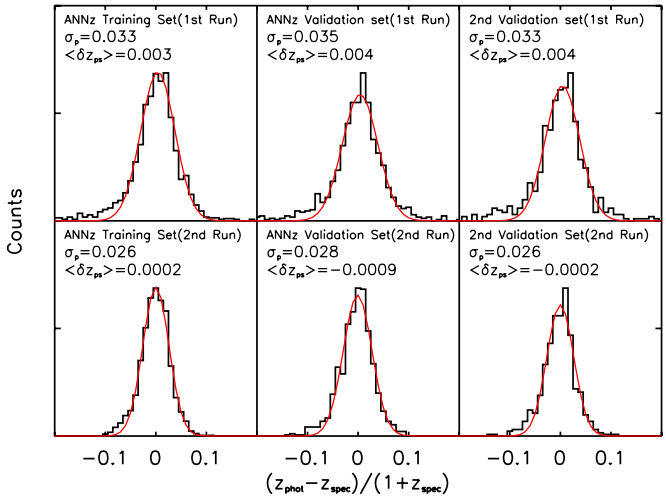

Figure 8. Histograms of photometric redshift errors $\delta z_p \equiv (z_{\rm phot} - z_{\rm spec})/(1 + z_{\rm spec})$. Panels from left to right show errors for the training, validation, and independent validation samples, respectively. Upper row shows the first ANNz estimation run, and the lower row shows the second run with flagged galaxies removed. Gaussian uncertainty σ_p and mean $(z_{\rm phot} - z_{\rm spec})/(1 + z_{\rm spec})$ for each set are indicated in each panel.

(A color version of this figure is available in the online journal.)

redshift errors, implying that a well-defined random uncertainty characterizes most of the photometric redshifts. Both the ANNz and independent validation sets yield similar $\sigma_p \sim 0.025$ in the second run, again with about 3.5% outliers. The training set σ_p cannot be used for an uncertainty estimate because it was deliberately minimized by the calculation. The outlier galaxies have a median 3.6 μm flux density of 12 μJy, much higher than the 6.5 μJy median flux density for the whole sample. The outlier galaxies with higher average 3.6 μm flux densities may have IRAC fluxes contaminated by nearby objects, or two sources are unresolved by IRAC but resolved at shorter wavelengths. The IRAC 3.6 μm image has a 2″ angular resolution, whereas the CFHT R-band images from which the DEEP2+3 sample was selected have resolution of ~1″. Contamination or source blending is therefore expected to occur.

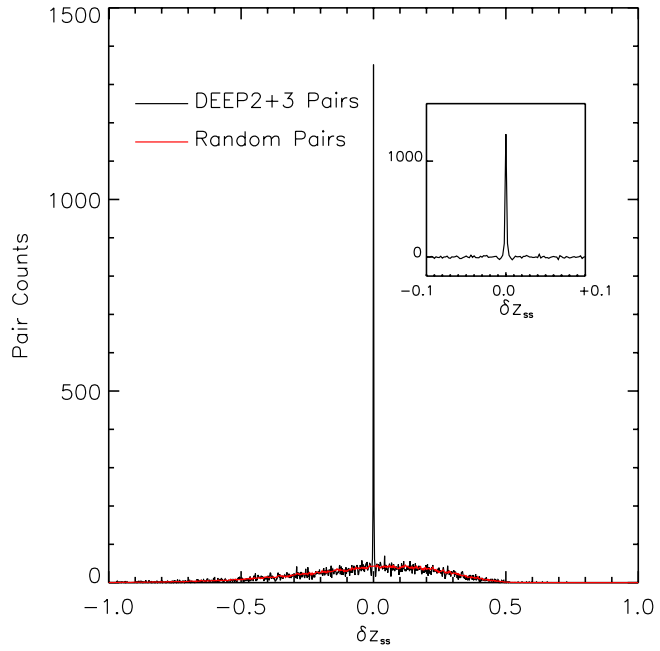

Figure 9. Histogram of normalized redshift offsets for galaxy pairs selected from the spectroscopic subsample. The red line shows the distribution expected for random, unrelated galaxies as calculated by a Monte Carlo simulation. The inset shows the residual real pair distribution after the random distribution of unrelated pairs is subtracted.

(A color version of this figure is available in the online journal.)

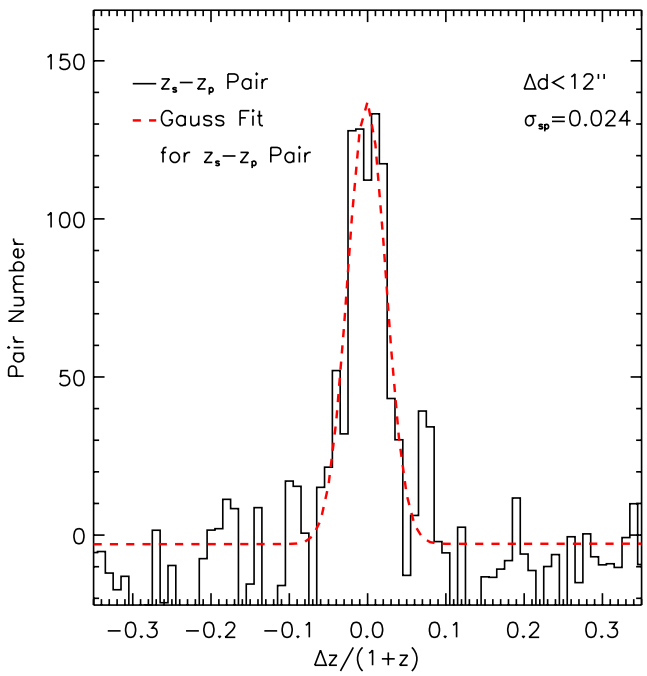

Figure 10. Histogram of normalized redshift offsets for galaxy pairs with one photometric and one spectroscopic redshift. The redshift offset distribution for the random, unrelated galaxy pair is already subtracted from the Monte Carlo simulation in this diagram. The red dashed line shows a Gaussian fit to the real pair distribution.

(A color version of this figure is available in the online journal.)

Galaxies with spectroscopic redshifts tend to be the brightest galaxies in any sample, and this is especially true in our 3.6 μm selected sample. Galaxies that are faint in visible light have relatively larger photometric errors and therefore may have larger errors in their photometric redshifts. Validation with the spectroscopic redshift subsample may not characterize the photometric redshift scatter for the fainter galaxies, and it is essential to assess photometric redshift accuracy for these faint objects.

We propose a new method to estimate the photometric redshift standard deviation for the whole sample. The method is based on galaxy–galaxy pair statistics. A substantial fraction of galaxy visual pairs are actually physically related, and the redshift offset for a real pair should be near zero. However, the calculated photometric redshift offset for a real pair may be nonzero if either redshift is erroneous. We define a visual pair as any two galaxies within an angular separation of 30″ and define the redshift offset as $\delta z_{\rm ss} \equiv (z_{\rm s1} - z_{\rm s2})/(1 + z_{\rm s1})$, where $z_{\rm s1}$ and $z_{\rm s2}$ are spectroscopic redshifts for two galaxies of the pair. The 30″ angular distance corresponds to a distance of 160–240 kpc for galaxies at $z = 0.4$–1.2, similar to the criterion of $d < 300$ kpc adopted by Lin et al. (2007) to study galaxy pairs and mergers in the same redshift range in the same field. Lin et al. (2007) found that these galaxy pairs have a very wide range of star formation activity. Galaxy pairs with shorter separation (∼50 kpc) likely have higher star formation activity, otherwise they do not show any bias toward any type.

Figure 9 shows the histogram of $\delta z_{\rm ss}$ for all visual pairs with both galaxies having redshifts in the DEEP2+3 sample. The histogram shows two components: a spike at $\delta z_{\rm ss} = 0$ for real pairs and a broad distribution for projected pairs that are physically unrelated. The expected $\delta z_{\rm ss}$ for projected pairs can be easily generated using Monte Carlo simulation and subtracted from the distribution for all pairs. The residual spike is the $\delta z_{\rm ss}$ distribution for real pairs. As expected, both of these velocity components are small compared to the expected uncertainty in the photometric redshifts.

Having a large number of spectroscopic redshifts available allows pair statistics to give a good estimate of the uncertainty in the ANNz redshifts. The pair sample tested consists of galaxies separated by <30″ where one galaxy has a spectroscopic redshift and the other only a photometric redshift. The normalized redshift offset is defined as $\delta z_{\rm sp} \equiv (z_p - z_s)/(1 + z_s)$, where z_p is the photometric redshift and z_s is the spectroscopic redshift of the respective galaxies. The histogram for all pairs (Figure 10) shows two components, as with spectroscopic pairs. Subtracting the simulated distribution for unrelated pairs from the real pair distribution gives the δz_{sp} distribution for physical pairs. This distribution shows a Gaussian shape (Figure 10) with $\sigma_{\rm sp} = 0.024$. This is very close to σ_p, the standard deviation of the photometric redshifts estimated from the difference between spectroscopic and photometric redshifts for the same galaxies.

The pair method can be used directly to validate the photometric redshifts for faint galaxies with $R > 24.1$. Figure 11 shows the results. $\delta z_{\rm sp}$ for these galaxies also shows a Gaussian shape with $\sigma_{\rm sp} = 0.024$. The pair statistics thus confirm the validity of the ANNz photometric redshifts even for galaxies fainter than the limiting magnitude of the training set.

Overall, σ_p of the photometric redshifts for the whole 3.6 μm sample is very close to that of recent state-of-the-art SED-fitting photometric redshifts for optically selected samples, which often have more than 20 bands of intermediate and broadband photometry (Wolf et al. 2003; Ilbert et al. 2006, 2009; Whitaker et al. 2011). Comparing with those photometric redshift estimations, the ANNz redshifts have well-defined and consistent error distributions for both optically bright and faint galaxies but are inherently limited to $z \leqslant 1.25$, the maximum redshift of the training set.

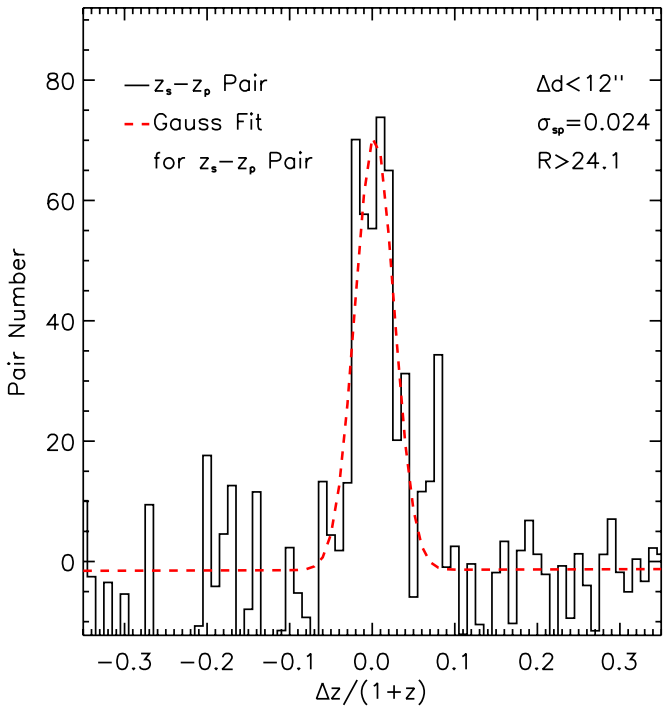

Figure 11. Histogram of normalized redshift offsets for galaxy pairs with one photometric and one spectroscopic redshift with the photometric component having $R > 24.1$. The redshift offset distribution for the random, unrelated galaxy pair is already subtracted with the Monte Carlo simulation in this diagram. The red dashed line shows a Gaussian fit to the real pair distribution.

(A color version of this figure is available in the online journal.)

4. GALAXY POPULATIONS IN THE 3.6 μm SELECTED SAMPLE

4.1. Color Classification

With redshifts known, deriving rest-frame colors and magnitudes for sample galaxies is straightforward. All types of galaxies have very similar SEDs at NIR wavelengths. The *K*-band absolute magnitudes for galaxies can therefore be calculated with the 3.6 μm flux densities and *K*-correction from De Propris et al. (2007). The absolute magnitude range for the sample is $-19 < M_K < -25$. Rest-frame $U - B$ colors for the sample were derived from $V - I$ colors via a set of local galaxy SED templates (Kinney et al. 1996—Willmer et al. 2006 and Faber et al. 2007 took a similar approach). Rest-frame absolute B magnitudes M_B were derived in the same way. The RS and BC (van Dokkum et al. 2000) were divided with the Willmer et al. (2006) criterion:

$$(U - B)_0 = -0.032(M_B + 21.52) + 0.454 - 0.25 + 0.832 \quad (4)$$

using the same U and B magnitude system they used but adding 0.832 to convert from the Vega to the AB system. Figure 12 shows a series of CM diagrams for the 3.6 μm selected sample.

Two types of galaxies have colors placing them in the RS: dusty star-forming galaxies and quiescent galaxies with little or no star formation (Labbe et al. 2005). Current studies use either a rest-frame visible color–color diagram or IR emission to separate these types (e.g., Brammer et al. 2009; Williams et al. 2009; Wang et al. 2012). Williams et al. (2009) showed that the types can be separated in a $U - V$ versus $V - J$ diagram, where dusty galaxies have redder $V - J$ colors than quiescent galaxies. Brammer et al. (2009) and Wang et al. (2012) used 24 μm emission to identify dusty star-forming galaxies. The 24–3.6 μm

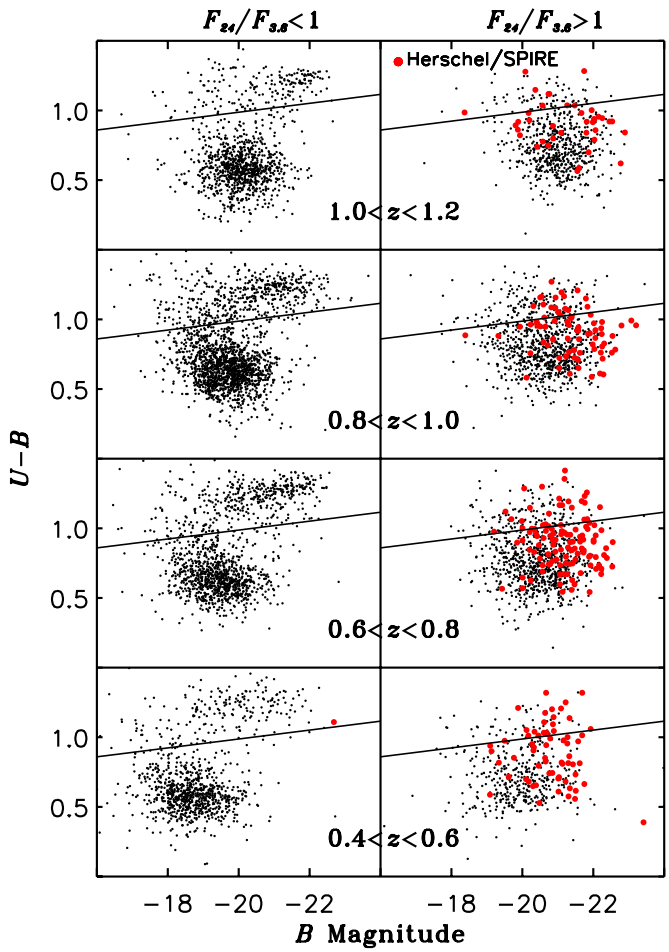

Figure 12. $U - B$ vs. M_B color–magnitude diagram for the 3.6 μm selected sample in redshift bins as indicated in the figure. The left panels are for non-dusty galaxies ($f_{24}/f_{3.6} < 1$), and right panels are for dusty galaxies ($f_{24}/f_{3.6} > 1$). The red dots denote *Herschel*/SPIRE sources selected at 250 μm (D. Rigopoulou et al., in preparation). Most of these sources are LIRGs or ULIRGs, and even some of the LIRGs and ULIRGs are in the red sequence.

(A color version of this figure is available in the online journal.)

flux density ratio, $f_{24}/f_{3.6}$, is closely related to the specific SFR and should therefore provide a good way of distinguishing passive from dusty star-forming galaxies. Figure 13 shows that $f_{24}/f_{3.6}$ is roughly constant for 24 μm sources with BC $U - B$ colors, but this ratio decreases to below 1 for 24 μm sources with RS colors. Nearly all 24 μm galaxies in the BC have $f_{24}/f_{3.6} > 1$, whereas more than 50% of 24 μm galaxies in the RS have $f_{24}/f_{3.6} < 1$. All *Herschel*/SPIRE sources in the RS also have $f_{24}/f_{3.6} > 1$. These sources must be star forming to be detected with SPIRE. We have therefore used $f_{24}/f_{3.6} = 1$ to separate dusty from passive galaxies in the RS: galaxies with $f_{24}/f_{3.6} < 1$ are taken to be passive galaxies with 24 μm residual emission, and galaxies with $f_{24}/f_{3.6} > 1$ in the RS are taken to be dusty and star forming. This criterion works because most RS galaxies in the sample are very luminous with $f_{3.6} > 20\,\mu$Jy and therefore RS galaxies not detected at 24 μm must have $f_{24}/f_{3.6} < 1$.

Galaxies with colors near the dividing line between the RS and the BC are called "green valley" objects. Most green valley galaxies are also MIPS 24 μm sources (Cowie et al. 2008; Kartaltepe et al. 2010). An IR-selected sample has many more green valley objects than a visible-selected sample, and this is the case for our 3.6 μm selected sample. Figure 12 shows many

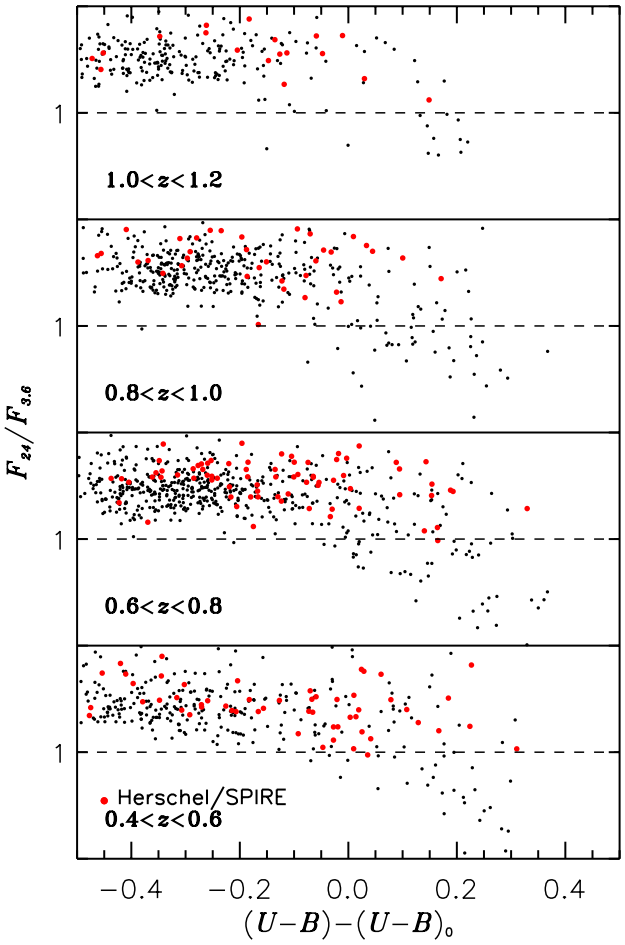

Figure 13. Infrared-visible color–color diagram for all galaxies in the 3.6 μm sample detected at 24 μm. Redshift bins are indicated. The abscissa is the $U - B$ color of each galaxy minus $(U - B)_0$ as given by Equation (4). Red dots denote *Herschel*/SPIRE sources detected at 250 μm (D. Rigopoulou et al., in preparation).

(A color version of this figure is available in the online journal.)

MIPS 24 μm sources in the green valley, and some are well into the RS color zone. On the other hand, most galaxies with no MIPS 24 μm detection have rest $U - B$ colors well away from the green valley, and the rest $U - B$ colors should accurately classify these galaxies as passive or star-forming.

4.2. Star Formation and Stellar Mass Assembly in the 3.6 μm Sample

Stellar mass for the 3.6 μm sample can be derived from stellar population models. In practice, we used BC03 (Bruzual & Charlot 2003) models with solar metallicity and Salpeter initial mass function (IMF). The model template set was generated with a grid of stellar masses, $E(B - V)$, ages, and e-folding times for star formation history. Stellar masses for the sample galaxies were determined by fitting their observed SEDs to the model templates. The derived stellar masses can be converted to those with the Chabrier IMF (Bundy et al. 2006) by adding −0.25 dex and to those with the "diet Salpeter" IMF (Bell et al. 2003) by adding −0.15 dex.

Even without detailed modeling, the rest-frame K-band luminosity for a galaxy is a good tracer of its stellar mass (e.g., Bell et al. 2003). The IRAC 3.6 μm band measures rest-frame K band for a galaxy at $0.4 < z < 1.2$. Figure 14 shows the K-band mass/light ratio for the galaxies in four redshift bins. The mass/light ratio is not constant but depends on color (as also found by Bell et al. 2003) and also slightly depends on redshift. Because the galaxies are bimodal in color, M/L also shows a bimodality: $M/L \sim 1.25$ for BC galaxies and $M/L \sim 3$ for RS galaxies. The different mass-light ratios imply different stellar mass limits in the 3.6 μm selected sample for the two galaxy classes.

Figure 15 shows galaxy color versus mass. In general, the most massive galaxies at any redshift are the red, quiescent ones. Those are followed by dusty star-forming galaxies, which are more massive than the remaining star-forming galaxies in the BC. Only the dusty star-forming galaxies are massive enough to be direct progenitors of massive red quiescent galaxies. Figure 15 also shows that there is a deficit of lower-mass RS galaxies at $1.0 < z < 1.2$. This is not a selection effect: galaxies with $M \approx 3 \times 10^9\ M_\odot$ would be readily detectable regardless of color. The deficit of low-mass galaxies on the RS at high redshift shows that the most massive RS galaxies formed first, many of them at $z > 1.2$. The high-redshift *Herschel*/SPIRE sources, representing LIRGs and ULIRGs, tend to be massive, indicating that intensive star formation occurs in massive galaxies at these redshifts.

Figure 16 shows galaxy color versus redshift in six stellar mass bins. Most galaxies in the highest mass bin are quiescent, indicating that they were already in place at $z = 1.2$. There are a few star-forming galaxies in this mass bin as well. On the other hand, the most intensive star formation was occurring in massive galaxies with $M_* > 10^{10}\ M_\odot$ at $0.4 < z < 1.2$. Figure 17 shows total infrared luminosities against stellar mass. The plot shows that most of the SPIRE sources are LIRGs or ULIRGs, and most are in the green valley (D. Rigopoulou et al., in preparation). Figure 17 is very similar to Figure 1 of Noeske et al. (2007) for the visible-selected spectroscopic sample in the same field, showing that more massive galaxies have higher total infrared luminosities. Yet the *Herschel*

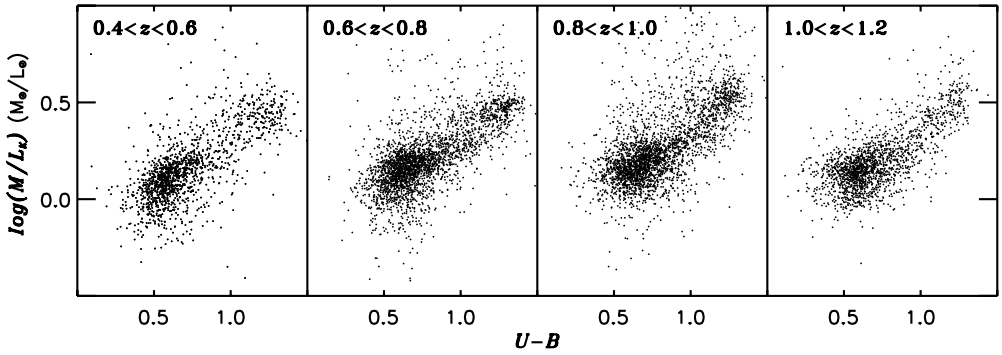

Figure 14. K-band mass/light ratio vs. $U - B$ color. Points denote all galaxies in the 3.6 μm selected sample. Redshift bins are indicated in each panel.

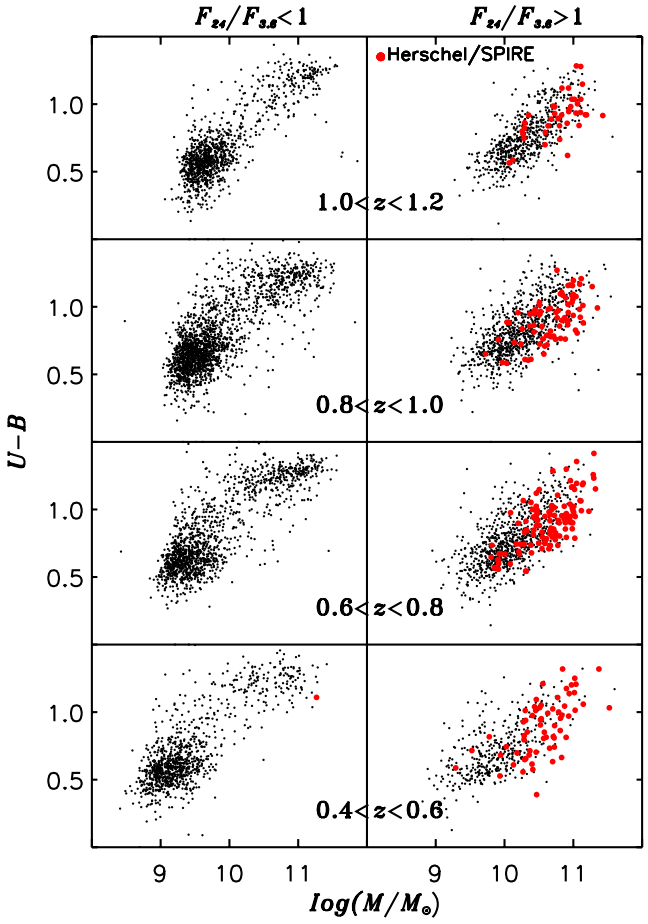

Figure 15. Color vs. stellar mass for the 3.6 μm sample. Redshift bins are indicated. The left panels are for non-dusty galaxies ($f_{24}/f_{3.6} < 1$), and right panels are for dusty galaxies ($f_{24}/f_{3.6} > 1$). The red dots denote *Herschel*/SPIRE sources selected at 250 μm (D. Rigopoulou et al., in preparation).

(A color version of this figure is available in the online journal.)

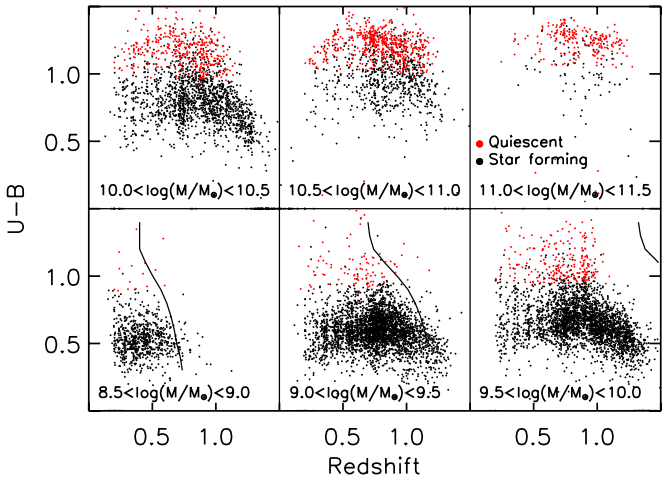

Figure 16. Color vs. redshift for the 3.6 μm sample. Stellar mass bins are indicated in each panel. The thick lines in the three lower panels indicate redshift limits to detect galaxies in these mass bins with typical colors. The limit ($z > 1.5$) is outside the diagram in the upper panels. Quiescent galaxies are absent at the high-redshift end in the three middle mass bins.

(A color version of this figure is available in the online journal.)

SPIRE-selected galaxies are biased toward the high L_{IR}, compared with the mean SFR–stellar-mass relation in the same redshift range for a more sensitive 24 μm selected sample (Elbaz et al. 2007). All of the ULIRGs are more massive than

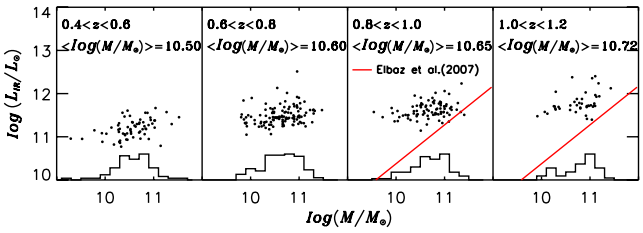

Figure 17. L_{IR}–stellar-mass relation for the *Herschel*/SPIRE sources in the 3.6 μm sample. Points denote individual galaxies with L_{IR} values from D. Rigopoulou et al. (in preparation). The red lines are the mean SFR–stellar-mass relation (converted to L_{IR}) for GOODS galaxies at $0.8 < z < 1.2$ (Elbaz et al. 2007). The *Herschel* galaxies are strongly biased toward the higher luminosity side. Redshift bins are indicated in each panel. Histograms show the stellar mass distribution of the SPIRE sources, and their median stellar mass is noted in each redshift bin.

(A color version of this figure is available in the online journal.)

$10^{10.5}$ $M_\odot$. The mean stellar mass for LIRGs/ULIRGs in the sample decreases from $10^{10.72}$ $M_\odot$ at $z = 1.1$–$10^{10.50}$ $M_\odot$ at $z = 0.5$, suggesting that more massive galaxies migrated to the RS earlier through intensive star formation.

Figure 16 also shows that quiescent galaxies at $z > 1.1$ are absent in the $10 < \log(M_*/M_\odot) < 10.5$ bin and so are those at $z > 1$ in the $9.5 < \log(M_*/M_\odot) < 10$ bin. This suggests that quiescent galaxies with low stellar mass did not form until low redshifts. Figure 18 shows the RS mass fraction as a function of redshift in each stellar bin. Though the mass fraction of quiescent galaxies in the $11 < \log(M_*/M_\odot) < 11.5$ bin has large error bars, it is ~75% and roughly constant from $z = 0$ to $z = 1$. This suggests that massive galaxies had largely stopped forming stars by $z = 1.2$. At $10.5 < \log(M_*/M_\odot) < 11$, the quiescent fraction increases from 40% at $z = 1.1$ to 60% at $z = 0.6$, close to the local value (58%; Bell et al. 2003) at $z \sim 0$. In the $10 < \log(M_*/M_\odot) < 10.5$ bin, the mass fraction increases from 10% at $z = 1.1$ to 30% at $z = 0.5$, also close to the local value of 41%. The x-intercept of this distribution is at $z \sim 1.3$. Quiescent galaxies in $9.5 < \log(M_*/M_\odot) < 10$ are a small fraction of the total at all epochs. The first such galaxies appeared around $z \approx 1.1$, and their numbers have increased to about 25% at $z \approx 0$.

There are two possible causes for the deficit of red quiescent galaxies in lower mass bins in Figure 18: (1) galaxies with lower mass migrated to the RS later; or (2) quiescent galaxies were undergoing either dry or mixed merging with high rate to move them quickly from lower mass end to high-mass end in the RS (Faber et al. 2007). The merging scenario requires such a high merging rate in low mass bins that galaxies just migrating to the RS were immediately undergoing dry/mixed merging. Yet Lin et al. (2008) found that fractions of dry and mixed mergers at $z \sim 1.1$ are only 8% and 24% for galaxies with a typical stellar mass of 2×10^{10} $M_\odot$. It is unlikely that the dry and mixed merging rate for galaxies with lower stellar masses would increase and be the major cause for the deficit of red quiescent galaxies in lower mass at $z \sim 1$.

In general, massive quiescent galaxies were already in place by $z = 1.2$, and quiescent galaxies with $9.5 < \log(M_*/M_\odot) < 10.5$ started to form in $1.1 < z < 1.3$. This indicates that the quenching of star formation, regardless of type, occurs earlier in massive galaxies and later in galaxies with lower stellar masses.

4.3. K-band Luminosity Function and Stellar Mass Functions

The rest K-band LF is an important measurement of galaxy population evolution. It is equivalent to a stellar mass function

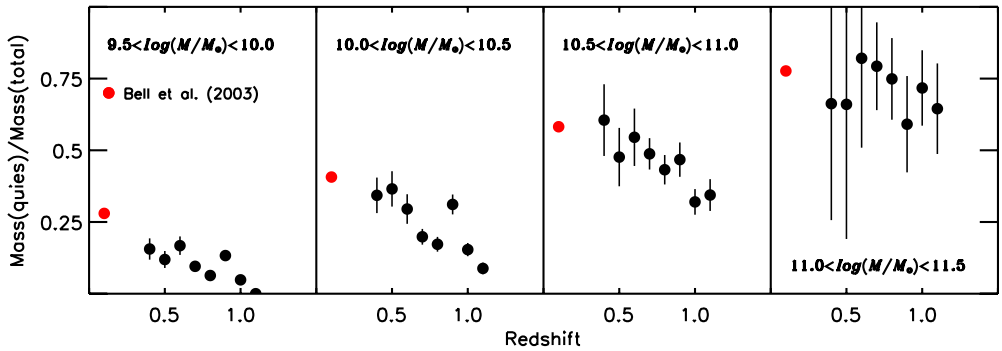

Figure 18. Fraction of quiescent galaxies as a function of redshift. Mass range is indicated for each panel. Black points denote the average mass fraction in small redshift ranges for the 3.6 μm sample, and red points denote the local value from Bell et al. (2003).

(A color version of this figure is available in the online journal.)

Table 2
EGS *K*-band Luminosity Function

	$0.4 < z < 0.6$		$0.6 < z < 0.8$		$0.8 < z < 1.0$		$1.0 < z < 1.2$	
K mag	$\log(\phi)$	$\delta\log(\phi)$	$\log(\phi)$	$\delta\log(\phi)$	$\log(\phi)$	$\delta\log(\phi)$	$\log(\phi)$	$\delta\log(\phi)$
−18.5	−2.67	0.30						
−19.0	−2.20	0.09	−3.24	0.44				
−19.5	−2.26	0.06	−2.43	0.06	−2.94	0.17		
−20.0	−2.29	0.07	−2.45	0.05	−2.42	0.05	−2.97	0.18
−20.5	−2.40	0.08	−2.53	0.05	−2.58	0.05	−2.73	0.06
−21.0	−2.56	0.09	−2.65	0.06	−2.67	0.05	−2.74	0.06
−21.5	−2.68	0.10	−2.73	0.06	−2.81	0.06	−2.82	0.06
−22.0	−2.64	0.10	−2.78	0.07	−2.81	0.06	−2.86	0.07
−22.5	−2.82	0.12	−2.81	0.07	−2.88	0.07	−2.99	0.08
−23.0	−2.79	0.12	−2.94	0.08	−2.98	0.07	−3.02	0.08
−23.5	−3.01	0.15	−3.00	0.09	−3.08	0.08	−3.15	0.09
−24.0	−3.43	0.25	−3.27	0.12	−3.32	0.11	−3.30	0.11
−24.5	−4.23	0.62	−3.91	0.25	−3.84	0.20	−3.90	0.22
−25.0			−4.71	0.62	−5.31	1.08	−4.96	0.76

but with a better defined completeness limit and much less model dependence. This is particularly true for our 3.6 μm selected sample. Because the IRAC 3.6 μm probes roughly the rest-frame *K* band for galaxies at $0.4 < z < 1.2$, the 3.6 μm-to-*K* *K*-correction is effectively independent of galaxy color, permitting an unbiased comparison of the LFs at different redshifts. We have derived the *K*-band LFs for quiescent, star-forming, and all galaxies in the EGS field at $z = 0.5$, 0.7, 0.9, and 1.1 with two methods: parametric and non-parametric. The non-parametric method is the familiar $1/V_{\rm max}$ (Felten 1976; Eales et al. 1993), and the parametric method is "STY" (Sandage et al. 1979), which fits a Schechter function to the sample. The STY method itself determines only α and M_K^* in the Schechter function. The normalization factor ϕ^* was derived using the minimum variance density estimator (Davis & Huchra 1982). Both LFs are plotted in Figure 20, and numerical values are given in Table 2.

The major uncertainty in an LF estimate based on a sample with small coverage or a single field is cosmic variance due to galaxy clustering (Huang et al. 1997; Somerville 2004; Newman & Davis 2002). Our *K*-band LFs were derived from a single $1^\circ \times 10'$ field. The maximum angular scale for this sample is 1°, and thus the cosmic-variance values, σ_v, at $z = 0.5$–1.1 are 28%–36% assuming a general correlation length $r_0 = 5$ Mpc (Somerville 2004). NIR-selected galaxies have a correlation length similar to that of visible-selected samples: Roche et al. (2003) and Oliver et al. (2004) measured correlation lengths of 4.1 and 6.4 Mpc for *K*- and IRAC-selected samples, respectively. Recently, Grazian et al. (2006) and Quadri et al. (2007) measured two-point correlation functions for distant red galaxies (DRGs) at $z \sim 2$ and obtained $r_0 = 7$–11 Mpc. The DRGs have a typical stellar mass of $10^{11}\ M_\odot$. If we adopted the largest $r_0 = 13.5$, the cosmic variance would be 2.5 times larger. However, this large correlation length is not applicable to the bulk of our sample but only to the most massive galaxies. The cosmic variance can also be calculated using dark matter variance and bias factor (Roche et al. 2003). The volumes for our sample in four redshift bins are ~ 1.2–2.8×10^5 Mpc^3, and within these volumes the dark matter fluctuation $\sigma_{\rm DM} \approx 0.25$. The number densities for L^* galaxies in our sample are 10^3 Mpc^{-3} (Figure 20), and therefore the bias for this population at $z \sim 1$ is $b \sim 1.5$. According to Roche et al. (2003), the cosmic variance $\sigma_v = b\sigma_{\rm DM}$, and $\sigma_v \sim 0.3$–0.4 for the L_* galaxies in our sample, consistent with values above. Thus all methods suggest that the variance for L^* galaxies in this sample is about 30%.

B-band LFs for galaxies at $0.4 < z < 1.2$ are well established both in the EGS and a wide range of other fields (Willmer et al. 2006; Faber et al. 2007). The comparison can be used to correct the EGS LF to the global average. The 3.6 μm sample is incomplete at faint *B* magnitudes (Figure 19). The 3.6 μm limiting magnitude is 23.2, corresponding to absolute magnitudes $M_K \approx -20$ to -21 at $0.4 < z < 1.2$. The rest-frame $B - K$ colors for galaxies are in the range of $-1 < B - K < 2$, giving a *B*-band completeness limit of -20.5 to -21.0. The mean density ratio between the EGS and global *B*-band LFs, taking into account only galaxies brighter than the

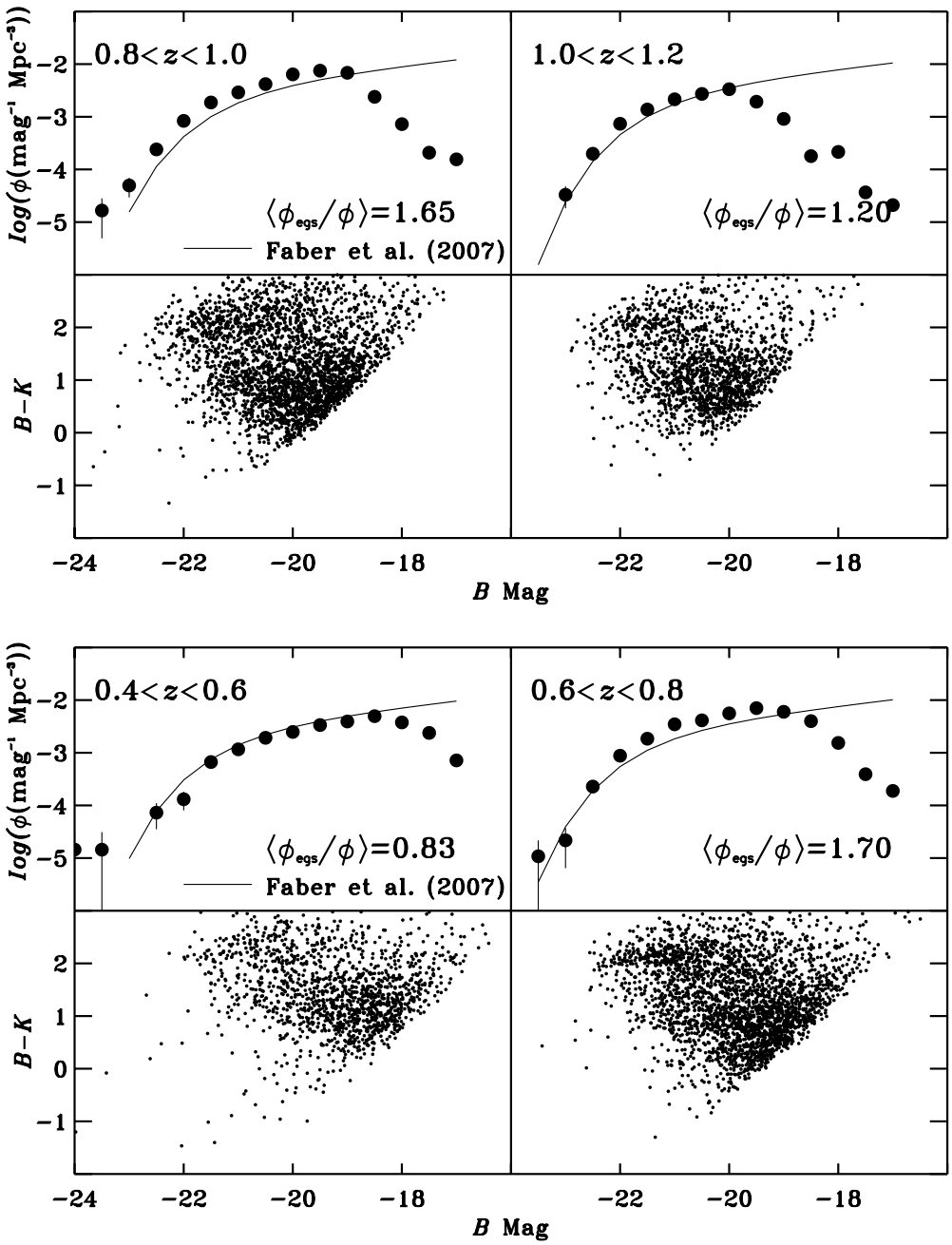

Figure 19. *B*-band luminosity functions (upper panels) and color–magnitude diagrams (lower panels). Redshift ranges are indicated. Points in the upper panels denote the luminosity function derived for the 3.6 μm sample, and lines show the luminosity function derived by Faber et al. (2007) from a visible sample. Points in the lower panels show color and magnitude for 3.6 μm selected galaxies. The absence of points in the lower right of the lower panels shows the incompleteness of the 3.6 μm sample for faint, blue galaxies.

completeness limit in each redshift bin, is $\langle\phi_{\rm egs}/\phi\rangle = 0.83$, 1.7, 1.66, and 1.20 for bins at $z = 0.5$, 0.7, 0.9, and 1.1, respectively. The standard deviation of these values is 0.38, consistent with the theoretical cosmic-variance estimation for this sample. The four values of $\langle\phi_{\rm egs}/\phi\rangle$ have been applied to the *K*-band LF and stellar mass function calculated for the 3.6 μm sample. The final LFs are plotted in Figure 20, and their values are given in Table 2. These corrected values should be representative of the entire universe, not the EGS field itself.

The VVDS (Le Fèvre et al. 2005) provides independent *K*-band LFs at $z = 0.5$, 0.7, 0.9, and 1.1. The VVDS itself measured redshifts in a wide area also covered by the *Spitzer* Wide-Area Infrared Extragalactic Survey (SWIRE; Lonsdale et al. 2004). Arnouts et al. (2007) used these data to derive *K*-band LFs in the same redshift bins we have used. Our *K*-band LFs are generally consistent with those of Arnouts et al., but the VVDS LFs at $z = 0.9$ and 1.1 are two times higher than ours at luminosities below L_*. We show later that the VVDS sample has higher mass densities for star-forming galaxies at $0.4 < z < 1.2$ than those obtained in any other survey and argue that the excess star-forming galaxies are the cause of their high *K*-band LFs at the faint end. Our *K*-band LFs and the VVDS ones with $L > L^*$ are higher than the local *K*-band LF (Huang et al. 2003; Jones et al. 2006). This is not due to number evolution for massive galaxies because massive galaxies can only increase in number toward lower redshifts. Thus, it implies a luminosity evolution in the *K* band from $z \sim 1$ to the present epoch.

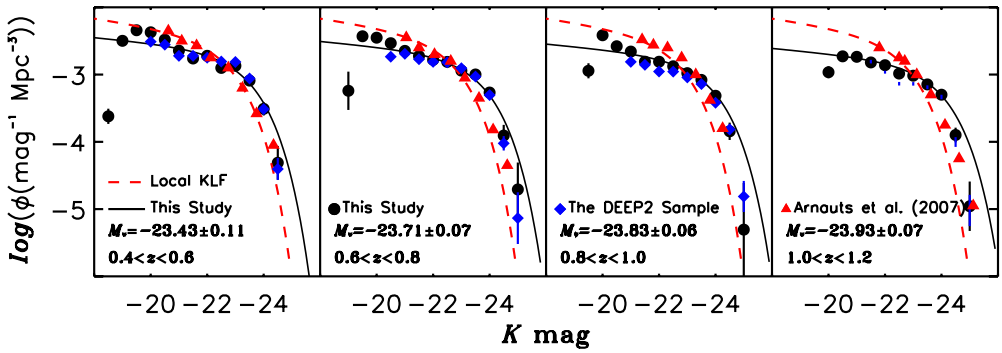

Figure 20. *K*-band luminosity functions. Blue points and solid lines show results from this study, while red points and dashed lines show comparisons from Jones et al. (2006) for the leftmost panel and Arnouts et al. (2007) for the other three panels. Redshift bins are indicated in each panel. The lines represent Schechter functions, the parameters of which are given in Table 2.

(A color version of this figure is available in the online journal.)

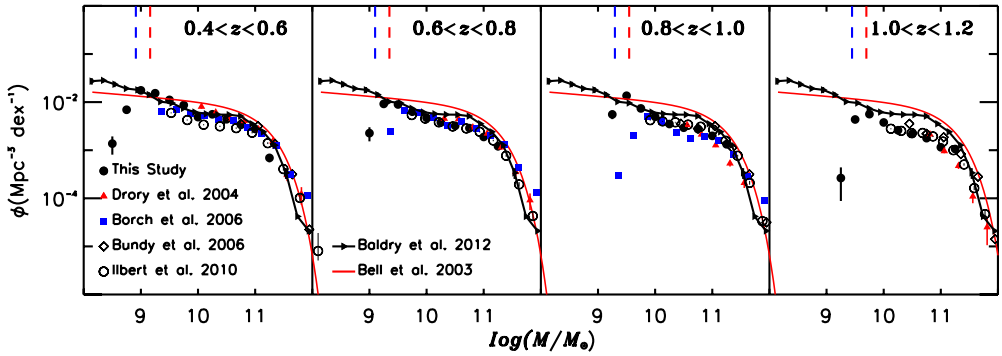

Figure 21. Stellar mass functions. Filled circles show results for the 3.6 μm selected sample. Other symbols show results for comparison samples as indicated in the figure legend. Red solid lines indicate the local stellar mass function in Bell et al. (2003), and black solid lines with arrow are the most updated local stellar mass function in Baldry et al. (2012). Vertical dashed lines indicate the completeness limits for the sample in each redshift bin, blue for star-forming galaxies and red for quiescent galaxies. Redshift bins are indicated in each panel.

(A color version of this figure is available in the online journal.)

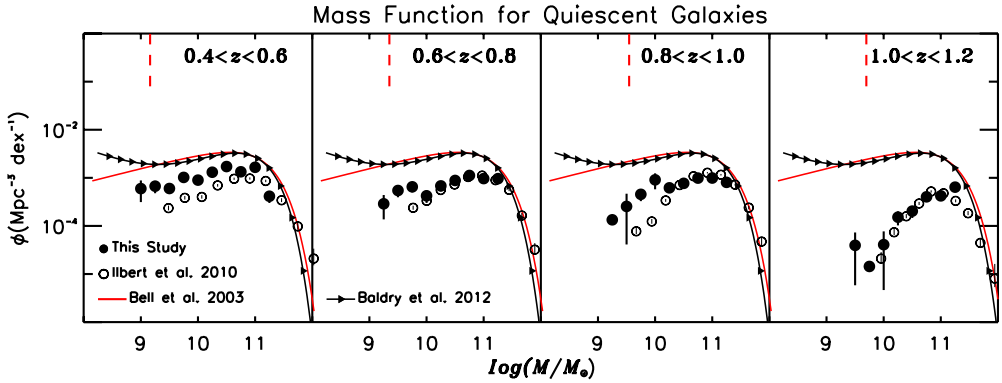

Figure 22. Stellar mass functions for quiescent galaxies. Filled circles show results for the 3.6 μm selected sample. Vertical dashed lines show the completeness limit of the sample. Open circles and open diamonds show results for quiescent galaxies in the COSMOS field (Ilbert et al. 2010). Redshift bins are indicated in each panel. Red solid lines show the local stellar mass function for quiescent galaxies in Bell et al. (2003), and black solid lines with arrows are the most updated local stellar mass function in Baldry et al. (2012).

(A color version of this figure is available in the online journal.)

Figures 21, 22, and 23, respectively, show stellar mass functions for all, quiescent, and star-forming galaxies with their values in Tables 3, 4, and 5. The mass-to-light ratios for quiescent and star-forming galaxies differ as shown in Figure 14 in the sense that the mass-to-light ratio for quiescent galaxies is roughly three times larger (Figure 14) than for star-forming galaxies. The survey mass limit for quiescent galaxies is therefore correspondingly larger for the fixed 3.6 μm limiting magnitude. At the low-mass end, star-forming galaxies are the dominant population in the 3.6 μm sample. Thus the mass limit for the whole sample should be very close to that for star-forming galaxies. Our stellar mass functions for the 3.6 μm selected sample are consistent with previous estimates (Drory et al. 2003; Borch et al. 2006; Bundy et al. 2006; Ilbert et al. 2010) but

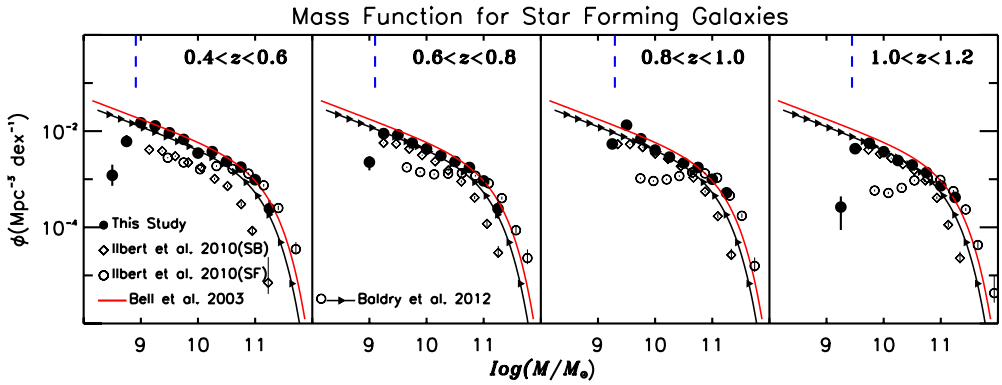

Figure 23. Stellar mass functions for star-forming galaxies. Filled circles show results for the 3.6 μm selected sample. Vertical dashed lines show the completeness limit of the sample. Open circles and open diamonds show results for star-forming and starburst galaxies in the COSMOS field (Ilbert et al. 2010). Redshift bins are indicated in each panel. Red solid lines show the local stellar mass function for star-forming galaxies (Bell et al. 2003), and black solid lines with arrows are the most updated local stellar mass function in Baldry et al. (2012).

(A color version of this figure is available in the online journal.)

Table 3
EGS Stellar Mass Function

	$0.4 < z < 0.6$		$0.6 < z < 0.8$		$0.8 < z < 1.0$		$1.0 < z < 1.2$	
$\log M_*$	$\log(\phi)$	$\delta\log(\phi)$	$\log(\phi)$	$\delta\log(\phi)$	$\log(\phi)$	$\delta\log(\phi)$	$\log(\phi)$	$\delta\log(\phi)$
9.00	−1.81	0.11	−2.65	0.22				
9.25	−1.87	0.09	−2.03	0.06	−2.27	0.14		
9.50	−2.01	0.07	−2.05	0.04	−1.88	0.07	−2.36	0.13
9.75	−2.12	0.08	−2.20	0.05	−2.14	0.06	−2.25	0.07
10.00	−2.37	0.10	−2.33	0.06	−2.32	0.07	−2.42	0.07
10.25	−2.31	0.10	−2.42	0.06	−2.47	0.06	−2.59	0.07
10.50	−2.41	0.11	−2.49	0.07	−2.54	0.06	−2.66	0.08
10.75	−2.52	0.13	−2.54	0.07	−2.57	0.07	−2.75	0.08
11.00	−2.61	0.14	−2.72	0.09	−2.71	0.08	−2.94	0.11
11.25	−3.22	0.28	−2.92	0.11	−2.89	0.10	−2.98	0.11

Table 4
EGS Stellar Mass Function for Quiescent Galaxies

	$0.4 < z < 0.6$		$0.6 < z < 0.8$		$0.8 < z < 1.0$		$1.0 < z < 1.2$	
$\log M_*$	$\log(\phi)$	$\delta\log(\phi)$	$\log(\phi)$	$\delta\log(\phi)$	$\log(\phi)$	$\delta\log(\phi)$	$\log(\phi)$	$\delta\log(\phi)$
9.00	−3.36	0.25						
9.25	−3.31	0.15	−3.34	0.14	−3.68	0.40		
9.50	−3.36	0.12	−3.06	0.08	−3.40	0.23	−4.32	0.31
9.75	−3.13	0.09	−2.98	0.06	−3.15	0.08	−4.76	0.41
10.00	−3.18	0.10	−3.17	0.08	−2.85	0.10	−4.31	0.32
10.25	−3.02	0.08	−2.96	0.06	−3.01	0.06	−3.74	0.12
10.50	−2.90	0.07	−2.85	0.05	−2.92	0.05	−3.61	0.10
10.75	−3.01	0.08	−2.75	0.05	−2.81	0.04	−3.32	0.07
11.00	−2.92	0.07	−2.81	0.05	−2.81	0.04	−3.30	0.07
11.25	−3.52	0.14	−2.81	0.05	−2.90	0.05	−3.11	0.06

Table 5
EGS Stellar Mass Function for Star-forming Galaxies

	$0.4 < z < 0.6$		$0.6 < z < 0.8$		$0.8 < z < 1.0$		$1.0 < z < 1.2$	
$\log M_*$	$\log(\phi)$	$\delta\log(\phi)$	$\log(\phi)$	$\delta\log(\phi)$	$\log(\phi)$	$\delta\log(\phi)$	$\log(\phi)$	$\delta\log(\phi)$
9.00	−1.91	0.05	−2.44	0.09	−4.45	0.41		
9.25	−1.97	0.02	−1.85	0.02	−2.07	0.06	−3.50	0.24
9.50	−2.11	0.03	−1.87	0.02	−1.68	0.03	−2.29	0.05
9.75	−2.25	0.03	−2.04	0.02	−1.97	0.03	−2.17	0.03
10.00	−2.54	0.05	−2.16	0.02	−2.20	0.03	−2.35	0.03
10.25	−2.51	0.05	−2.31	0.03	−2.35	0.03	−2.53	0.03
10.50	−2.71	0.06	−2.43	0.03	−2.47	0.03	−2.62	0.03
10.75	−2.83	0.07	−2.55	0.04	−2.56	0.03	−2.78	0.04
11.00	−3.09	0.09	−2.83	0.05	−2.81	0.04	−3.06	0.05
11.25	−3.69	0.18	−3.41	0.10	−3.09	0.08	−3.30	0.07

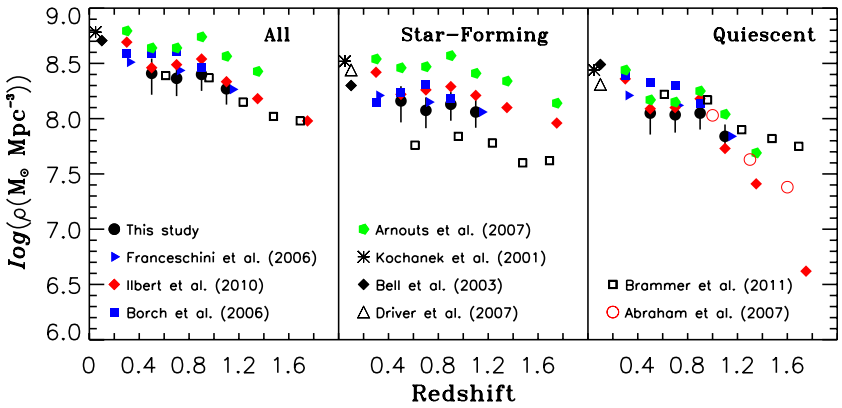

Figure 24. Stellar mass density as a function of redshift. Black filled circles show results for this study, and other symbols show other results as indicated in the figure legends. Panels show total, star-forming, and quiescent galaxies, respectively, but different authors have used different criteria to separate the latter two classes.
(A color version of this figure is available in the online journal.)

extend below $10^{9.5}$ $M_{\odot}$, the lowest stellar mass range so far explored at these redshifts. Our stellar mass functions for star-forming galaxies are consistent with those in the COSMOS field (Ilbert et al. 2010) except in the bin of $0.4 < z < 0.6$, where the COSMOS stellar mass function is lower at $\log(M_*/M_{\odot}) < 10.5$. The mass functions for quiescent galaxies in the EGS and COSMOS fields are consistent with each other at the massive end, but our mass functions for quiescent galaxies are higher at the lower mass end. Our EGS sample is probably more complete for faint red galaxies because the IRAC exposure time is nine times longer than that of COSMOS.

In comparison with the local stellar mass function (Bell et al. 2003; Baldry et al. 2012), our stellar mass function shows number evolution since $z = 1.1$. We also measured the stellar mass densities for galaxies with $\log(M_*/M_{\odot}) > 9.5$ in each redshift bin (Figure 24). The total stellar mass density increased by a factor of 3–5 from $z = 1.1$ to $z \sim 0.1$ (Kochanek et al. 2001; Bell et al. 2003; Driver et al. 2007). In contrast, our mass function for high-z star-forming galaxies is similar to local mass functions (Bell et al. 2003; Driver et al. 2007; Figure 23), implying very weak evolution. The number of star-forming galaxies at the lower mass end has increased only slightly since $z = 1$. The stellar mass function for quiescent galaxies shows two different evolutions in Figure 22: the absolute number of massive quiescent galaxies and the slope of the low-mass end both increase at low redshifts. This indicates that massive quiescent galaxies were still forming at $z < 1$, and most low-mass quiescent galaxies formed much later than their massive counterparts.

The composite stellar mass functions show number evolution since $z = 1.1$ (Figure 21), indicating continuing mass assembly since that epoch. The star-forming galaxy population shows little evolution, and thus the quiescent population is mainly responsible for the evolution in the composite mass functions. The quiescent galaxies came from the star-forming galaxy population, and the amount of mass assembled in star-forming galaxies is roughly the same as the mass migrating from the BC to the RS. Such mass assembly can also be seen in the stellar mass density as a function of redshift. Several groups (Bell et al. 2003; Borch et al. 2006; Franceschini et al. 2006; Abraham et al. 2007; Arnouts et al. 2007; Ilbert et al. 2010) have used stellar mass densities as a function of redshift to demonstrate how stellar masses were assembled in galaxies over time (Figure 24). Our stellar mass densities for both populations are consistent with the other measurements, and indeed all surveys yield roughly similar mass densities in the redshift range of $0.4 < z < 1.1$ (Figure 24). The mass densities for star-forming galaxies have large scatter: the VVDS has the highest (Arnouts et al. 2007) and the NEWFIRM has the lowest (Ilbert et al. 2010). All surveys yield similar quiescent galaxy mass densities within a factor of two in this redshift range. This is simply due to better photometric redshifts for quiescent galaxies than star-forming galaxies. The overall mass densities increase by a factor of ~4 from $z = 1.2$ to $z = 0$, and the mass densities for quiescent galaxies also increased by a factor of 5–8 since $z = 1.2$.

5. SUMMARY

A multi-wavelength study of a 3.6 μm selected galaxy sample at $0.4 < z < 1.2$ with $f_{3.6} > 2\,\mu$Jy in the EGS region has allowed a new suite of photometric redshifts based on a neural network method. The distribution of $(z_p - z_s/1 + z_s)$ is Gaussian with $\sigma \sim 0.025$. Pair statistics validates the photometric redshifts even for galaxies too faint to obtain spectroscopic redshifts and shows that the redshifts have scatter similar to that for the brighter galaxies. The rate of catastrophic redshift failures is about 3.5%.

Basic properties measured for the galaxy sample include rest-frame $U - B$ colors, B- and K-band absolute magnitudes, and stellar masses for galaxies in the sample. In the redshift range available, the IRAC 3.6 μm band probes the rest-frame near-infrared, permitting sample selection based on stellar mass and only weakly biased with respect to quiescent and star-forming galaxies. Our sample is complete for galaxies with $\log(M_*/M_{\odot}) > 9.5$ at $0.4 < z < 1.2$. We divided the sample into quiescent and star-forming galaxies according to their rest-frame $U - B$ color and $f_{24}/f_{3.6}$ flux ratio. We then derived K-band LFs and stellar mass functions for quiescent, star-forming, and all galaxies in the sample at $z = 0.5$, 0.7, 0.9, and 1.1.

Our conclusions are as follows.

1. The $U - B$ versus B CM diagram cannot by itself efficiently separate quiescent and star-forming galaxies. There are MIPS 24 μm sources in the RS in the CM diagram. About half of these sources have $f_{24}/f_{3.6} > 1$, indicating that they are dusty star-forming galaxies. The remaining objects have $f_{24}/f_{3.6} < 1$, which indicates quiescent galaxies with residual star formation or AGN activities.
2. The $U - B$–mass diagram shows an absence of quiescent galaxies with $\log(M_*/M_{\odot}) < 10$ at $1.0 < z < 1.2$. The

quiescent galaxy mass fractions at low masses ($9.5 < \log(M_*/M_\odot) < 10.5$) increase with cosmic time from 0%–10% at $z = 1.1$ to 25%–35% at $z = 0.5$. These quiescent galaxies probably first started to appear at $z \sim 1.3$. In comparison, for galaxies an order of magnitude more massive ($10.5 < \log(M_*/M_\odot) < 11$), the quiescent fraction was already 50% of the total stellar mass at $z = 1.1$, and this fraction has increased only to ~60% at $z \sim 0$.

3. Throughout the redshift range $0.4 < z < 1.2$, ~70% of the massive galaxies ($\log(M_*/M_\odot) > 11$) are quiescent. These massive quiescent galaxies can have formed in one of two ways: either they come directly from star-forming galaxies with similar masses but much shorter life times, or they resulted from lower-mass RS galaxies merging. Some massive galaxies are in a ULIRG phase, giving support to the first scenario.
4. We derived the *K*-band LFs and stellar mass functions in four redshift bins. The cosmic variance in EGS has been corrected by comparing the EGS *B*-band LFs with the global *B*-band LFs. Our *K*-band LFs suggest that there may be a luminosity evolution in the *K* band, which needs to be confirmed with larger samples. There is number evolution in the stellar mass function, which increases from $z = 1.1$ to $z = 0$. Yet the stellar mass function for star-forming galaxies shows very weak evolution compared to strong evolution in quiescent galaxies. This implies that the amount of mass assembled in star-forming galaxies is roughly the same as the amount of mass in galaxies migrating from the BC to the RS. The faint-end slope for the quiescent galaxy mass function has increased since $z = 1.1$, indicating that lower mass quiescent galaxies formed much later. The mean mass density increased roughly a factor of three from $z = 1.1$ to $z = 0$.

This work is based in part on observations made with the *Spitzer Space Telescope*, which is operated by the Jet Propulsion Laboratory, California Institute of Technology under a contract with NASA. Support for this work was provided by NASA through an award issued by JPL/Caltech. Part of the work was done during J.-S. Huang's visit to Shanghai Normal University supported by the Chinese National Nature Science foundation Nos. 10878003 and 10833005.

Facilities: Spitzer (IRAC, MIPS), Subaru

REFERENCES

Abraham, R. G., Nair, P., McCarthy, P. J., et al. 2007, ApJ, 669, 184
Arnouts, S., Walcher, C. J., Le Févre, O., et al. 2007, A&A, 467, 137
Baldry, I. K., Driver, S. P., Loveday, J., et al. 2012, MNRAS, 421, 621
Barmby, P., Huang, J.-S., Ashby, M. L. N., et al. 2008, ApJS, 177, 431
Barro, G., Pérez-González, P. G., Gallego, J., et al. 2011, ApJS, 193, 13
Bell, E., McIntosh, D. H., Katz, N., & Weinberg, M. D. 2003, ApJS, 149, 289
Bell, E., Naab, T., McIntosh, D. H., et al. 2006, ApJ, 640, 241
Bell, E., Wolf, C., Meisenheimer, K., et al. 2004, ApJ, 608, 752
Bell, E. F., & de Jong, R. S. 2001, ApJ, 550, 212
Borch, A., Meisenheimer, K., Bell, E. F., et al. 2006, A&A, 453, 869
Brammer, G. B., Whitaker, K. E., van Dokkum, P. G., et al. 2009, ApJL, 703, L173
Brodwin, M., Brown, M. J. I., Ashby, M. L. N., et al. 2006, ApJ, 651, 791
Bruzual, G., & Charlot, S. 2003, MNRAS, 344, 1000
Bundy, K., Ellis, R. S., Conselice, C. J., et al. 2006, ApJ, 651, 120
Cimatti, A., Mignoli, M., Daddi, E., et al. 2002, A&A, 392, 395
Cohen, J. 2002, ApJ, 567, 672
Cole, S., & Lacey, C. 1996, MNRAS, 281, 716
Cole, S., Norberg, P., Baugh, C. M., et al. 2001, MNRAS, 326, 255
Collister, A. A., & Lahav, O. 2004, PASP, 116, 345
Cooper, M. C., Aird, J. A., Coil, A. L., et al. 2011, ApJS, 193, 14
Cooper, M. C., Griffith, R. L., Newman, J. A., et al. 2012, MNRAS, 419, 3018
Cowie, L. L., & Barger, A. L. 2008, ApJ, 686, 72
Cowie, L. L., Songaila, A., Hu, E. M., & Cohen, J. G. 1996, AJ, 112, 839
Davis, M., Faber, S. M., Newman, J., et al. 2003, Proc. SPIE, 4834, 161
Davis, M., Guhathakurta, P., Konidaris, N. P., et al. 2007, ApJ, 660, 1
Davis, M., & Huchra, J. P. 1982, ApJ, 254, 437
Desai, V., Soifer, B. T., Dey, A., et al. 2009, ApJ, 700, 1190
De Propris, R., Stanford, S. A., Eisenhardt, P. R., Holden, B. P., & Rosati, P. 2007, AJ, 133, 2209
Dickinson, M., & FIDEL Team, 2007, BAAS, 39, 822
Driver, S. P., Allen, P. D., Liske, J., & Graham, A. W. 2007, ApJL, 657, L85
Drory, N., Bender, R., Feulner, G., et al. 2003, ApJ, 595, 698
Eales, S. 1993, ApJ, 404, 51
Elbaz, D., Daddi, E., Le Borgne, D., et al. 2007, A&A, 468, 33
Faber, S., Willmer, C. N. A., Wolf, C., et al. 2007, ApJ, 665, 265
Fadda, D., Yan, L., Lagache, G., et al. 2010, ApJ, 719, 425
Felten, J. E. 1976, ApJ, 207, 700
Firth, A. E., Lahav, O., & Somerville, R. S. 2003, MNRAS, 339, 1195
Franceschini, A., Rodighiero, G., Cassata, P., et al. 2006, A&A, 453, 397
Franx, M., Labbé, I., Rudnick, G., et al. 2003, ApJ, 587, 79
Grazian, A., Fontana, A., Moscardini, L., et al. 2006, A&A, 453, 507
Hogg, D. W., Blanton, M. R., Eisenstein, D. J., et al. 2003, ApJ, 585, 5
Hopkins, P., Hernquist, L., Cox, T. J., et al. 2006, ApJS, 163, 1
Huang, J.-S., Barmby, P., Fazio, G. G., et al. 2004, ApJS, 154, 44
Huang, J.-S., Cowie, L. L., Gardner, J. P., et al. 1997, ApJ, 476, 12
Huang, J.-S., Faber, S. M., Daddi, E., et al. 2009, ApJ, 700, 183
Huang, J.-S., Glazebrook, K., Cowie, L. L., & Tinney, C. 2003, ApJ, 584, 203
Huang, J.-S., Rigopoulou, D., Papovich, C., et al. 2007, ApJ, 660, 69
Huang, J.-S., Rigopoulou, D., Willner, S. P., et al. 2005, ApJ, 634, 137
Ilbert, O., Arnouts, S., McCracken, H. J., et al. 2006, A&A, 457, 841
Ilbert, O., Capak, P., Salvato, M., et al. 2009, ApJ, 690, 1236
Ilbert, O., Salvato, M., Le Floc'h, E., et al. 2010, ApJ, 709, 644
Im, M., Simard, L., Faber, S. M., et al. 2002, ApJ, 571, 136
Ivison, R., Chapman, S. C., Faber, S. M., et al. 2007, ApJL, 660, L71
Jones, H. D., Peterson, B. A., Colless, M., & Saunders, W. 2006, MNRAS, 369, 25
Kartaltepe, J. S., Sanders, D. B., Le Floc'h, E., et al. 2010, ApJ, 721, 98
Kauffmann, G., Heckman, T. M., White, S. D. M., et al. 2003a, MNRAS, 341, 33
Kauffmann, G., Heckman, T. M., White, S. D. M., et al. 2003b, MNRAS, 341, 54
Kauffmann, G., White, S. D. M., & Guiderdoni, B. 1993, MNRAS, 264, 201
Kinney, A. L., Calzetti, D., Bohlin, R. C., et al. 1996, ApJ, 467, 38
Kochanek, C. S., Pahre, M. A., Falco, E. E., et al. 2001, ApJ, 560, 566
Labbe, I., Huang, J., Franx, M., et al. 2005, ApJ, 624, 81
Laird, E., Nandra, K., Georgakakis, A., et al. 2009, ApJS, 180, 102
Laird, E., et al. 2012, in preparation
Le Fèvre, O., Vettolani, G., Garilli, B., et al. 2005, A&A, 439, 845
Lilly, S., Le Févre, O., Renzini, A., et al. 2007, ApJS, 172, 70
Lilly, S., Tresse, L., Hammer, F., Crampton, D., & Le Fevre, O. 1995, ApJ, 455, 108
Lin, H., Yee, H. K. C., Carlberg, R. G., et al. 1999, ApJ, 518, 533
Lin, L., Koo, D. C., Weiner, B. J., et al. 2007, ApJL , 660, L51
Lin, L., Patton, D. R., Koo, D. C., et al. 2008, ApJ, 681, 232
Lonsdale, C., Polletta, M., Surace, J., et al. 2004, ApJS, 154, 54
Lotz, J. M., Davis, M., Faber, S. M., et al. 2008, ApJ, 672, 177
Lu, N., Helou, G., Werner, M. W., et al. 2003, ApJ, 588, 199
Madgwick, D. S., Coil, A. L., Conselice, C. J., et al. 2003, ApJ, 599, 997
McCracken, H. J., Capak, P., Salvato, M., et al. 2010, ApJ, 708, 202
Nandra, P., et al. 2006, in preparation
Newman, J. A., & Davis, M. 2002, ApJ, 564, 567
Noeske, K., Weiner, B. J., Faber, S. M., et al. 2007, ApJL, 660, L43
Oliver, S. J., Bock, J., Altieri, B., et al. 2012, MNRAS, 424, 1614
Oliver, S. J., Waddington, I., Gonzalez-Solares, E., et al. 2004, MNRAS, 154, 30
Oliver, S. J., Wang, L., Smith, A. J., et al. 2010, A&A, 518, 21
Quadri, R., van Dokkum, P., Gawiser, E., et al. 2007, ApJ, 654, 138
Rigopoulou, D., Huang, J.-S., Papovich, C., et al. 2006, ApJ, 648, 81
Roche, N. D., Dunlop, J., & Almaini, O. 2003, MNRAS
Roseboom, I. G., Ivison, R. J., Greve, T. R., et al. 2012, MNRAS, 419, 2758
Rudnick, G., Franx, M., Rix, H.-W., et al. 2001, AJ, 122, 2205
Sandage, A. R., Tammann, G. A., & Yahil, A. 1979, ApJ, 232, 352
Shapley, A., Steidel, C. C., Erb, D. K., et al. 2005, ApJ, 626, 698
Smith, A. J., Wang, L., Oliver, S. J., et al. 2012, MNRAS, 419, 377
Somerville, R., Lee, K., Ferguson, H., et al. 2004, ApJL, 600, L171
Somerville, R. 2005, NewAR, 49, 366
Sorba, R., & Sawicki, M. 2010, ApJ, 721, 1056

Steidel, C., Adelberger, K. L., Shapley, A. E., et al. 2003, ApJ, 592, 728
Steidel, C., Shapley, A. E., Pettini, M., et al. 2004, ApJ, 604, 534
Stern, D., Eisenhardt, P., Gorjian, V., et al. 2005, ApJ, 631, 163
Strateva, I., Ivezić, Ž., Knapp, G. R., et al. 2001, AJ, 122, 1861
Taylor, E. N., Franx, M., van Dokkum, P. G., et al. 2009, ApJS, 183, 295
Toomre, A., & Toomre, J. 1972, ApJ, 178, 623
Toth, G., & Ostriker, J. P. 1992, ApJ, 398, 5
Wang, T., Huang, J.-S., Faber, S. M., et al. 2012, ApJ, 752, 134
Weedman, D., Polletta, M., Lonsdale, C. J., et al. 2006, ApJ, 653, 101
Whitaker, K. E., Labbé, I., van Dokkum, P. G., et al. 2011, ApJ, 735, 86
Williams, R. J., Quadri, R. F., Franx, M., van Dokkum, P., & Labbé, I. 2009, ApJ, 691, 1879
Willmer, C. A. N., Faber, S. M., Koo, D. C., et al. 2006, ApJ, 647, 853
Wolf, C., Meisenheimer, K., Rix, H.-W., et al. 2003, A&A, 401, 73
van Dokkum, P., Franx, M., Fabricant, D., Illingworth, G. D., & Kelson, D. D. 2000, ApJ, 541, 95
van Dokkum, P., Labbé, I., Marchesini, D., et al. 2009, PASP, 121, 2
Zhao, Y. H., Huang, J.-S., Ashby, M., Fazio, G., & Miyazaki, S. 2009, RAA, 9, 1061